RIVISTA DEL NUOVO CIMENTO Vol. 28, N. 12 2005
DOI 10.1393/ncr/i2006-10010-8

Photoluminescence of rare-earth–doped glasses

G. C. Righini([1])(*) and M. Ferrari([2])(**)

([1]) *Istituto di Fisica Applicata "Nello Carrara" and Dipartimento Materiali e Dispositivi CNR - Via Madonna del Piano 10, 50019 Sesto Fiorentino (Firenze), Italy*

([2]) *CSMFO Group, Istituto di Fotonica e Nanotecnologie, CNR, Sezione di Trento Via Sommarive 14, 38050 Povo (Trento), Italy*

(ricevuto il 13 Marzo 2006)

Summary. — Rare-earth elements are of interest in several high-tech and environmental application areas, the two major ones concerning magnetic and optical devices. In the latter field, one can exploit the unique photoluminescence properties of rare-earth ions to develop novel or advanced lasers and optical amplifiers. Glasses have been known for a long time as a convenient host for rare earths and have been widely used for the fabrication of solid-state lasers. Recently, guided-wave format has added several advantages, namely the small size, the high pump power density, and the larger flexibility in design and fabrication. Thus, in the last few years, due to the great development of optical communications, an increasing research and development activity has been focused on the design and manufacture of fibre optic and integrated optic lasers and amplifiers, especially of those based on Er^{3+}-doped glasses. The aim of the present paper is to highlight the application of the spectroscopic techniques to the characterization of rare-earth–doped glasses and to present a brief overview of the efforts and progresses made in the area of micro-optic and integrated-optic lasers and amplifiers. A brief summary of the fundamentals of the photoluminescence properties and of the measurements techniques is also provided.

PACS 78.55.-m – Photoluminescence, properties and materials.
PACS 42.62.Fi – Laser spectroscopy.
PACS 42.70.-a – Optical materials.
PACS 42.82.-m – Integrated optics.

(*) E-mail: giancarlo.righini@cnr.it
(**) E-mail: mferrari@science.unitn.it

2 1. Introduction
5 2. Rare-earth–doped glasses
7 3. Spectroscopic techniques for optical materials assessment
7 3˙1. Absorption measurements
9 3˙1.1. Absorption spectroscopy for OH^- content assessment
11 3˙2. Luminescence measurements
13 3˙3. Raman and Brillouin scattering for optical-glasses characterization
20 4. Absorption and emission cross-section measurement
25 5. Quantum efficiency evaluation
28 6. Radiation trapping, self-absorption and concentration-quenching phenomena
31 7. Photonic band gap structures with glassy materials
33 8. Rare-earth–doped glasses for lasers and amplifiers
33 8˙1. Integrated optical amplifiers
36 8˙2. Optical and spectroscopic properties of Er^{3+}-doped waveguides
38 8˙2.1. Sol-gel silica-hafnia films
39 8˙2.2. Soda-lime-alumino-silicate (SLAS) glasses
41 8˙2.3. Tellurite glass waveguides
42 9. Microspherical lasers
45 10. Conclusions and perspectives

1. – Introduction

Photoluminescence (PL) is the emission of light from a material under optical excitation. It is one of the kinds of the more general phenomenon of luminescence, namely the emission of optical radiation resulting from various types of excitation: chemical or biochemical changes, electrical energy, subatomic motions, reactions in crystals, or stimulation of an atomic system. Accordingly, one can speak about bio-, chemi-, electro-, thermo-, radio-luminescence, and so on.

When light of sufficient energy is incident on a material, photons are absorbed and electronic excitations are created. Eventually, the electrons return to the ground state: if this relaxation is radiative, the emitted light is the photoluminescence signal. The intensity of this signal gives a measure of the relative rates of radiative and nonradiative recombinations.

Often one can also refer to fluorescence or phosphorence: the latter is a type of luminescence that occurs naturally in many minerals and metallic compounds, in some organic compounds, and in some living organisms such as marine fauna and insects (the most familiar one being the firefly, whose light flashes are produced by biochemiluminescence). Phosphorescence is distinguished from fluorescence for two main reasons: a) in phosphorence there is a longer time period between the excitation and the emission of light; b) phosphorescence may continue for some time (even hours) after the exciting source has been removed, while fluorescence ceases when excitation is off.

Photoluminescence effects have been observed for thousands of years; the oldest known written observations on bioluminescent phenomena in nature were made in China, dating roughly from 1500 to 1000 B.C. regarding fireflies and glow-worms. Only during the 16th and 17th centuries, in Europe, the first efforts were made to understand and apply such phenomena. Indeed, the first object of scientific study of luminescent phenomena was a natural stone, subsequently referred to as the “Bolognian Phosphorus” or “Bolognian Stone” or “Litheophosphorus”, which had been discovered in 1602 on Monte Paderno,

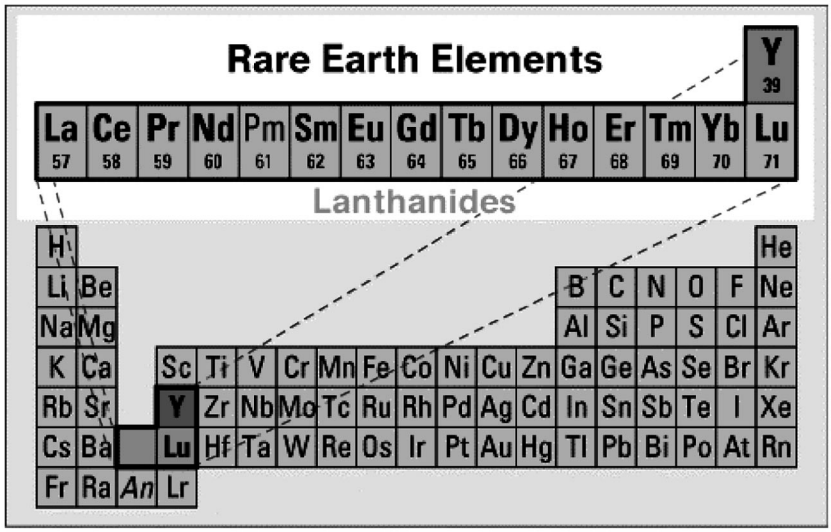

Fig. 1. – Position of the rare-earth elements in the periodic table of elements.

just outside of Bologna, Italy, by Vincenzo Casciarolo, an amateur alchemist [1]. The beginning of luminescence science, however, can be dated to 1852, when George Stokes interpreted the light-emitting phenomenon and formulated the law (the Stokes Law or the Stokes Shift) that the fluorescent light is of longer wavelength than the exciting light [2]. It was Stokes who coined, in 1853, the term "fluorescence" from *fluor*spar (calcium fluoride), the name of the mineral where he first noticed the phenomenon, and the ending *-escence* analogous to opalescence, phosphorescence, etc.

Nowadays, photoluminescence is mostly exploited for materials' characterization: from the analysis of the PL signal one can derive much information on the emitting material, and PL may be particularly useful in surface diagnostic, because the phenomenon often originates from the surface layers of the material. A noticeable advantage of PL analysis is that it is a simple, versatile, and non-destructive technique. Obviously, PL depends much on the nature of the optical excitation, as the excitation energy selects the initial photoexcited state and governs the penetration depth of the incident light.

Among the materials that can be usefully investigated by using PL techniques, an important class is that of rare-earth–doped glasses. Their impact is mostly related to the development of optical communications and to the recent request of increasing the bandwidth capacity of optical fibre systems.

The rare-earth elements (REEs) form the largest chemically coherent group in the periodic table (fig. 1); though generally not so well known, because of their specificity, REEs have many high-tech and environmental applications. Europium, for instance, is used as the red phosphor in colour cathode-ray tubes and liquid-crystal displays. Alloys containing one REE (such as Nd, Sm, Gd, Dy, Pr) have revolutionized the permanent magnet technology. Forefront research is now looking at the properties of the unique magnetic-martensitic phase transformation in R_5T_4 materials (where R is Gd and other rare earths and T, for instance, is Si, Ge, or Sn) in order to understand the underlying electronic structure and the microscopic interactions bringing extremely strong coupling of the magnetic moments with the lattice [3]. A better understanding of this phase trans-

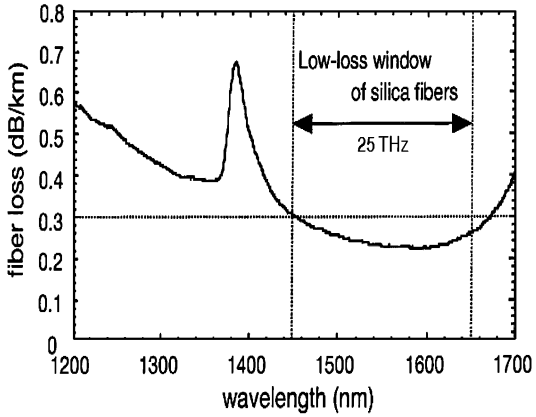

Fig. 2. – Transmission curve in the near-infrared region of a typical single-mode fibre for optical communication systems.

formation and other basic phenomena may lead to the development of novel material systems exhibiting extremely large magnetocaloric, magnetostrictive, and magnetoresistance responses to small changes of magnetic field, temperature, and pressure. Even environmental applications of REEs have grown significantly over the past decades. REEs, for instance, are essential constituents of automotive catalytic converters. Widespread use of new energy-efficient fluorescent lamps (using Y, La, Ce, Eu, Gd, and Tb) may alleviate energy consumption. Large-scale application of magnetic-refrigeration technology, based on a "giant magnetocaloric effect" near room temperature exhibited by the $Gd_5(Si_2Ge_2)$ alloy, also could significantly reduce energy consumption and CO_2 emissions.

Coming to the field of optics, cerium, the most abundant and least expensive element in the group, is very much appreciated as polishing agent for glass. Neodymium is very well known as the active dopant of glass or YAG (yttrium aluminium garnet) for solid-state lasers. The most popular application of REEs over the last decades, however, has been that of the development of fibre and integrated-optics lasers and amplifiers [4, 5].

Erbium (alone or together with ytterbium) in glass or other dielectric materials (such as lithium niobate) has become one of the key materials in photonic systems. Its relevance is due to two factors: i) the optical amplifier (OA) is a key enabling technology to achieve the high-speed and high-volume transmission required in current optical transmission systems [4-6]; and ii) the photoluminescence peak of Er is at a wavelength around $1.5\,\mu$m, just inside the so-called third window of fibre communication systems. The broadness of the amplification band is of particular concern nowadays; let us refer to fig. 2, which shows the typical transmission curve of a single-mode commercial silica fibre for optical communications. The low-loss window (if we choose the 0.3 dB/km threshold) is over 200 nm wide ($\approx$ 25 THz); by exploiting this entire band it would be easy to achieve multi-Tb/s transmission. In fact, by using a 0.4 nm (or $\approx$ 50 GHz) channel spacing—as is done currently in DWDM (dense wavelength division multiplexing) systems—one could allocate 500 communication channels, each one with a transmission speed over 10 Gb/s, thus making system bit rates over 5 Tb/s possible. Not only erbium, however, is important for communication systems; for instance, the first 10 Tb/s WDM transmission in single fibre was demonstrated in 2001 by using a gain-shifted thulium-doped fibre amplifier in a system using 273 50-GHz–spaced channels, each with 40 Gb/s capacity [7].

This paper is intended to serve both as an introduction to the field of photoluminescence techniques applied to rare-earth–doped glasses and as a review of recent works aiming, on the one hand, at the characterization of novel glasses and, on another hand, at the development of integrated optical devices exploiting such properties. By necessity, this review is not exhaustive, and we have only attempted to offer the non-specialized reader a brief overview of the ongoing activities and of the problems to be faced in this field.

2. – Rare-earth–doped glasses

Oxide glasses are well known as excellent hosts for rare-earth ions: one of the first solid-state lasers was demonstrated in 1961 in Nd^{3+}-doped glass [8]. Lasing in a Nd^{3+}-doped multi-component glass fibre was reported three years later [9]. The same material structure was exploited to demonstrate the first thin-film waveguide glass amplifier, in 1972 [10], and the first integrated optical glass laser, in 1974 [11]. The interest for Er^{3+}-doped glasses arose quite later, in the late 1980s, when the main operational wavelength for optical-fibre communication systems shifted towards the $1.5\,\mu$m band [12]. Since then, many remarkable results in the development of more efficient glass matrices and in the actual fabrication of rare-earth–doped (RED) glass integrated optical amplifiers have been achieved.

RE (lanthanide) ions are characterized by $[Xe].4f^{12}.6s^2$ electronic configuration; all of them have the same outer-shell configuration, namely $5s^25p^66s^2$. The most stable ionisation state is the trivalent one, with the $5s$ and $5p$ electrons remaining untouched and acting to screen the energy levels of the $4f$ electrons from the effect of the surrounding environment. The transition probabilities between $4f$ states, however, are sensitive to the ions surrounding the rare earth, and the design of a proper RED glass involves the study of a number of spectroscopic parameters. The Judd-Ofelt theory [13, 14] is usually adopted to calculate, by assuming certain approximations, transition probabilities from the data of absorption cross-sections of several f-f transitions. According to this theory, the strength of an f-f transition may be expressed by the sum of the products of three intensity parameters Ω_i ($i = 2, 4, 6$) times the squared matrix elements $U(i)$ between the initial J-states and the terminal J' state. Once the phenomenological parameters Ω_i have been calculated, it is possible to derive the strength of any absorption or emission transition, as well as the stimulated emission cross-section, the fluorescence branching ratio from level J to J', and the radiative lifetime of an excited level. Radiative lifetime, however, may be calculated even in a simpler way, by using Einstein relation for the transition probability between absorption and emission coefficients; this issue will be treated in more detail in the following section. The energy levels of the RE ions are shown in fig. 3.

One of the major limits to the quantum efficiency η of a given transition in a RE ion in a glass, defined as the ratio between the measured fluorescence lifetime τ_{meas} and the radiative lifetime τ_{rad} of the excited state, is constituted by nonradiative relaxations, that in turn may be classified as a) multiphonon relaxations; b) cross relaxations; and c) cooperative upconversion processes. Phonon relaxations correspond to the collisional decay of an excited energy level, due to the crystalline lattice vibrations or, in other words, to the rapid short-range movement of the closely spaced atoms. Multiphonon relaxations between two energy states occur by the simultaneous emission of several phonons that are sufficient to conserve the energy of the transition. Table I reports typical phonon energies of different glass matrices; the probability of multiphonon relaxation may be assessed by

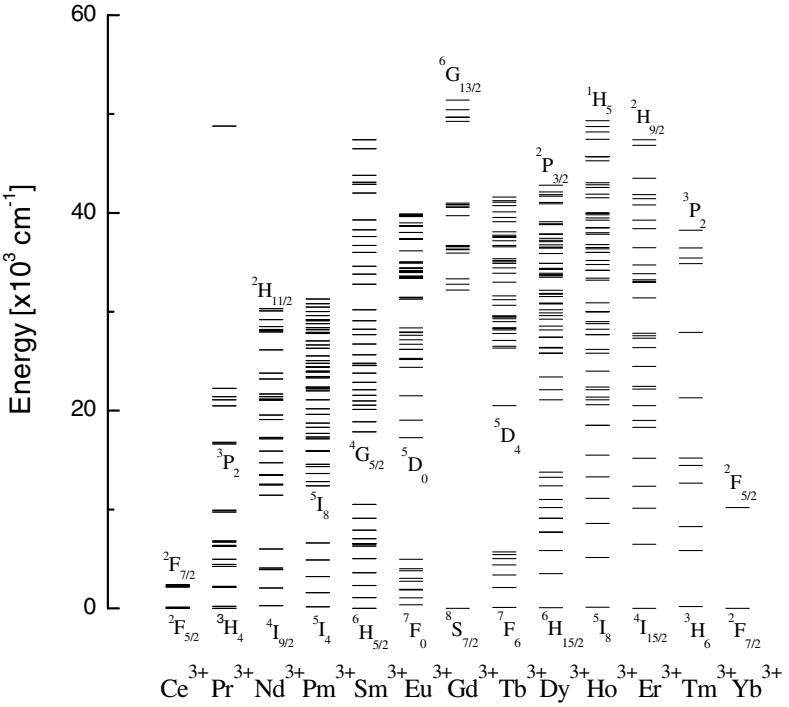

Fig. 3. – Energy levels of trivalent rare-earth ions. Electronic energies were determined on the basis of published data [100].

using a simple energy gap model [15]. The multiphonon decay rates as a function of energy gap to the next lower level have been measured experimentally for silicate glasses doped with Nd^{3+}, Er^{3+}, Pr^{3+} and Tm^{3+}; it was found that an approximately exponential dependence holds, independently of the RE ion or electronic level [16].

Cross relaxations and cooperative upconversion processes, on the other hand, lead to fluorescence quenching, *i.e.* to the decrease of fluorescence intensity when the RE concentration is increased. One has to consider, in fact, that, with increasing concentration of RE ions, the ion spacing decreases and may be small enough to allow them

TABLE I. – *Maximum phonon energy of various glass matrices.*

Glass	Phonon energy (cm^{-1})
Borate	~ 1400
Phosphate	1100–1200
Silicate	~ 1100
Germanate	~ 900
Tellurite	~ 700
Fluorozirconate	~ 500
Sulfide (Ga, La)	~ 450

to interact and transfer energy. Cross relaxation may occur between RE ions of the same type if they have two pairs of energy levels characterized by the same energy gap ΔE. An excited ion A (donor) transfers half of its energy to a ground-state ion B (acceptor), so that both ions move to a same intermediate level, from which they decay non-radiatively to the ground level. It appears that this kind of dissipative phenomenon is the major responsible of concentration quenching of Nd^{3+} through the energy transfers $Nd^{3+}(^4F_{3/2} \downarrow {}^4I_{15/2}) \Rightarrow Nd^{3+}(^4F_{9/2} \uparrow {}^4I_{15/2})$; subsequent relaxation from $^4I_{15/2}$ to $^4F_{9/2}$ occurs via phonons. Co-operative up-conversion process occurs between two excited ions A and B: A gives its energy to B, so that A relaxes to ground state, while B goes to a higher energy level. From this higher level B can relax either emitting a photon with higher energy (*i.e.* higher frequency and lower wavelength) than the exciting photon—it is this case which gave the "up-conversion" label to the process—or via phonons and a lower-energy photon. In any case, at least one exciting photon is lost for the amplifying process, and fluorescence quenching in Er^{3+} may be primarily attributed to this process.

The interested reader is referred for further details to the many precious books published on the physics of glass lasers [5, 17-21].

3. – Spectroscopic techniques for optical materials assessment

The aim of this section is to recollect some basics concerning the use of spectroscopic techniques such as absorption, luminescence, Raman and Brillouin spectroscopy for the study of optical materials. Particular attention is being paid to their application to thin films and planar waveguides activated by various optically active elements, in particular rare-earth ions; some interesting aspects related to massive systems will be discussed as well. The interest of absorption and luminescence spectroscopy is obvious in photonics. These two techniques, in particular, allow one to determine the spectroscopic properties of the optical species imbedded in a matrix [22-24]. The spectroscopic and optical techniques are currently used for optimization and pre-competitive fabrication of innovative devices. The fundamentals of optical spectroscopy, both theoretical and experimental, can be found in several textbooks and scientific papers, *e.g.*, in [22-27] and references therein. The spectroscopic properties, namely emission quantum efficiency, lifetime of the excited electronic states, dynamical processes, etc., of systems activated by luminescent ions are investigated by luminescence spectroscopy. The typical experimental configuration used to study the spectroscopic properties of a planar waveguide is shown in fig. 4. This set-up is practically the same one used in m-line spectroscopy, where the light is injected into the film by prism coupling [28, 29]. This configuration allows an appreciable increase of contrast, as well as selectivity of both mode and polarization. Detailed discussions about the waveguiding geometry are reported in several books and review articles [30-32].

3˙1. *Absorption measurements.* – Absorption spectra are fundamental to determine the factors governing several properties of optical materials, such as losses, absorption cross-sections and refractive index. The simplest schema is to measure the decrease of the optical intensity of the beam travelling the material as a function of the wavelength λ. In the linear behaviour, the absorption coefficient α for a sample of thickness L is given by the Lambert-Beers law:

$$I(\lambda) = I_0(\lambda) \exp[-\alpha(\lambda) L], \tag{3.1.1}$$

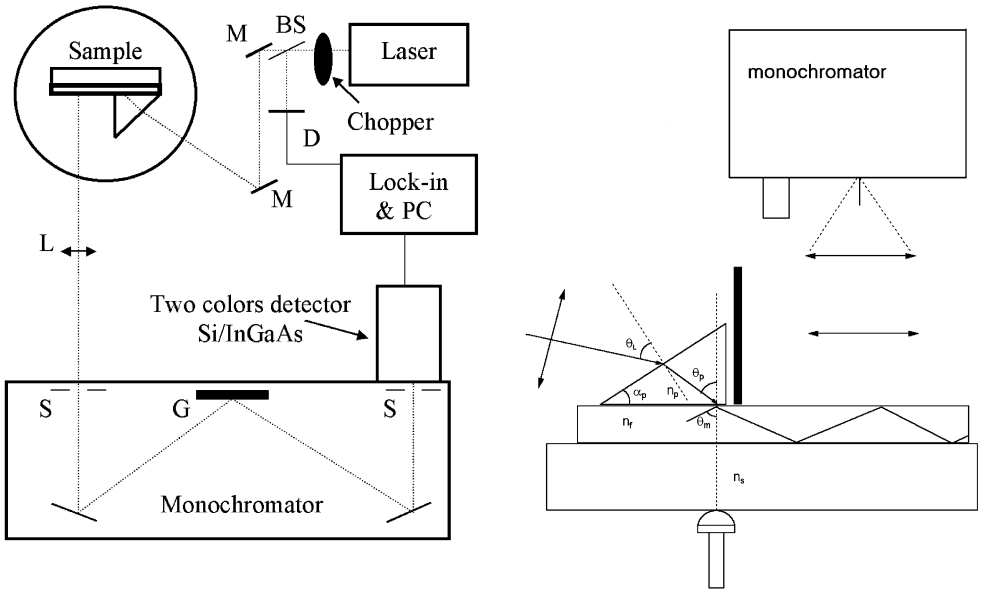

Fig. 4. – Experimental set-up used for luminescence measurements in waveguide configuration. The laser light is injected into the guide by prism coupling, as in the typical arrangement used for m-line spectroscopy: slits (S); grating (G); lens (L); mirror (M); beam splitter (BS); reference diode (D). Adapted from [77].

where I is the intensity measured after an optical path length L, and I_0 is the intensity incident on the sample. Because L has the dimension of a length (L), the absorption coefficient α has dimension L^{-1} and it is usually measured in cm^{-1}. The absorption coefficient is related to the imaginary part of the refractive index $n_i(\lambda)$ by

$$\alpha(\lambda) = \frac{4\pi}{\lambda} n_i(\lambda). \tag{3.1.2}$$

In the discussion of the absorption spectra, other quantities are currently used:

Transmission:

$$T(\lambda) = \frac{I(\lambda)}{I_0(\lambda)}\,. \tag{3.1.3}$$

Optical density or absorbance:

$$OD(\lambda) = -\log(T(\lambda)) \quad \text{or} \quad T(\lambda) = 10^{-OD(\lambda)}. \tag{3.1.4}$$

Extinction coefficient:

$$\varepsilon(\lambda) = \frac{\alpha(\lambda)}{C} = -\frac{\log(T(\lambda))}{C \cdot L}\,, \tag{3.1.5}$$

where C is the concentration measured in $\mathrm{mol\,l^{-1}}$. The units of the extinction coefficient or molar absorptivity are $\mathrm{mol^{-1}\,l\,cm^{-1}}$.

Absorption cross-section:

$$\sigma(\lambda) = \frac{\alpha(\lambda)}{N}\,, \tag{3.1.6}$$

where N is the density of the absorbing centres given in $\mathrm{cm^{-3}}$ unit. The absorption cross-section quantifies the ability of an ion to absorb light and is one of the most common values used in photonics for sample characterization. The amount of power absorbed by an ion when light is incident upon it at wavelength λ is given by

$$P(\lambda) = \sigma(\lambda) I(\lambda), \tag{3.1.7}$$

where I is the intensity of the light incident upon the ion, given in Watt $\mathrm{cm^{-2}}$. The dimension of σ is that of an area. The cross-section can be thought of as a sort of target area that can intercept a light flux by catching the photons that flow through it.

The extinction coefficient and the cross-section are related by

$$\varepsilon(\lambda) = \sigma(\lambda)\frac{N_{\mathrm{A}}}{\ln 10} \cong l \cdot \sigma(\lambda) \cdot 2.6154 \cdot 10^{20}, \tag{3.1.8}$$

where $N_{\mathrm{A}} = 6.0221367\,10^{23}\,\mathrm{mol^{-1}}$ is Avogadro's number.

The absorption coefficient can be measured in $\mathrm{dB\,cm^{-1}}$ by the equation

$$I(\lambda) = I_0(\lambda) 10^{-\frac{\gamma}{10}L}, \tag{3.1.9}$$

where γ is the attenuation coefficient expressed in $\mathrm{dB\,cm^{-1}}$. Comparing the expressions used for γ ($\mathrm{dB\,cm^{-1}}$) and α ($\mathrm{cm^{-1}}$), it results that the two values are related by

$$\gamma = 4.343\ \alpha. \tag{3.1.10}$$

An exhaustive presentation of the optical theory applied to infrared absorption spectroscopy is reported in [33].

3˙1.1. Absorption spectroscopy for OH^- content assessment. Let us now refer to some applications where absorption, transmission and reflectance spectra play an important role in characterization of materials. Absorption spectroscopy is largely employed in chemical sensing, often in conjunction with optical fibres or planar waveguides [34-37]. An important example, where infrared absorption measurements can give useful information on optical materials, concerns the estimation of OH^- content in rare-earth–activated glasses. The O-H stretching vibration affects the fluorescence decay of Er^{3+} ions at $1.5\,\mu$m because two O-H vibrations are enough to bridge the gap of about $6500\,\mathrm{cm^{-1}}$ between the ground state, ${}^4I_{15/2}$, and the first excited state, ${}^4I_{13/2}$, of the Er^{3+} ion [22, 38-41]. The consequence of the presence of residual OH^- species in the material is a strong reduction of the quantum efficiency of the ${}^4I_{13/2}$ level. Although the presence of OH^- group is the main determinant of the performance of sol-gel–based devices, because it is intrinsic to the sol-gel processing, the detrimental non-radiative relaxation channel due to vibrations of OH^- groups is effective also in melt-derived glasses.

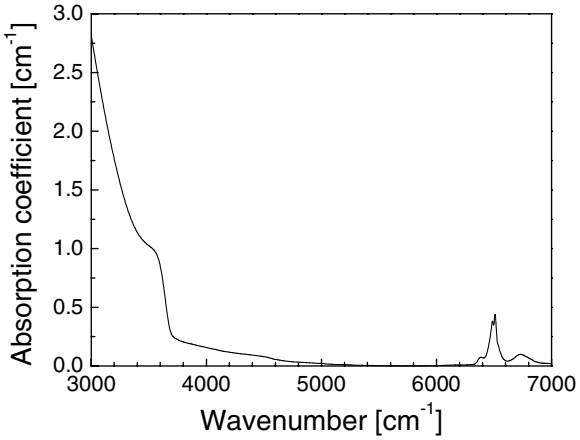

Fig. 5. – Room temperature FTIR absorption spectrum of a Er^{3+}-activated silicate glass (77.29 SiO_2: 11.86 K_2O: 10.37 PbO: 0.48 Sb_2O_3) in the IR region [42].

Figure 5 shows the absorption spectrum of a glass produced at Cristallerie Baccarat by a conventional melt-quenching technique with the following molar composition: 77.29 SiO_2: 11.86 K_2O: 10.37 PbO: 0.48 Sb_2O_3 and activated by Er^{3+} ions [42]. The spectrum shows the multiphonon tail of the absorption edge, which partially overlaps the wide band (3000–3700 cm^{-1}) assigned to the presence of hydroxyl groups in the glass matrix, centred at about 3570 cm^{-1} [43, 44]. The amplitude of this fundamental OH^- stretching band allows the estimation of the OH^- concentration by the Beer-Lambert law $C = (\alpha \times 0.434)(1/\varepsilon)$, where C is the concentration of the bonded species whose vibrations induce the IR light absorption, α is the absorption coefficient and ε is the extinction coefficient. A rough estimation of water content is obtained assuming that the value of the extinction coefficient is comparable to what it is found for aluminosilicate glasses ($\varepsilon_{3520\,nm} = 40\,l_{glass}/mol_{OH}\,cm_{glass}$) [43] and andesitic glasses ($\varepsilon_{3570\,nm} = 70 \pm 0.7\,l_{glass}/mol_{OH}\,cm_{glass}$) [44, 45]. Taking a value of the extinction coefficient $\varepsilon_{3570\,nm} \sim 70\,l_{glass}/mol_{OH}\,cm_{glass}$ and $\alpha \sim 1\,cm^{-1}$, the resulting C_{OH} concentration is as low as $6 \times 10^{-6}\,mol\,cm^{-3}$, which corresponds to an OH^- content of about $3.6 \times 10^{18}\,cm^{-3}$.

Another well-established procedure to determine the hydroxyl content is the so-called "baseline absorbance method", developed by Heigl *et al.* at Esso Laboratories in 1947 for the analysis of hydrocarbon mixtures [46]. The intensity of absorption of the individual peaks associated with the specific chemical species, which are chosen in order to minimize the interference between two or more compounds, is expressed as "base-line" optical density. This is calculated from the equation $OD_{Base} = -\log \frac{I}{I_{Base}}$, where OD_{Base} is the base line optical density, I is the absorption intensity measured as the distance from the zero line to the selected absorption peak, and I_{Base} is the distance from zero line to a straight line, the base line, joining two spectral points located on either side of the absorption peak. This equation is a modification of eq. (3.1.4), by the substitution of I_{Base}, the zero to base-line distance, for I_0, the incident light intensity. The base-line points are selected after the most favourable analytical peaks have been determined, and in the standard absorption spectra the base line is drawn parallel to the background. The method was applied first by Pope and Mackenzie to determine the hydroxyl content

of densified Nd^{3+}-activated silica glass prepared by the sol-gel route [47]. Taking into account the OH^- transmission at 2.6 μm (T_a) and 2.7 μm (T_b), respectively, the relation $[OH](ppm) = (1000/d)\log(T_a/T_b)$ allowed the estimation of the OH^- content in a sample with a thickness d [46, 47].

Both the two methods described above are based on the proportionality between concentration and absorption peak; they can be applied to a wide variety of samples, and permit a satisfactory accuracy. A detailed discussion concerning the infrared spectroscopy study of water-related species in silica glasses can be found in [48, 49], and a phenomenological model for the OH^- absorption effect to the attenuation coefficient in telecommunication fibres is reported in [50].

3˙2. *Luminescence measurements.* – In material systems activated by cromophores ions, the spectroscopic properties, such as emission quantum efficiency, lifetime of the excited electronic states, and dynamical processes such as non-radiative relaxation mechanism, upconversion and cooperative processes [51], may be well investigated by luminescence spectroscopy.

Rare-earth–doped glasses are used in a large number of optical devices because of the large number of absorption and emission bands available using the various rare-earth elements [52, 53]. As an example, the variation in the green intensity ratio between the $^2H_{11/2}$ and $^4S_{3/2}$ energy levels to the ground state of Er^{3+} ions has been used as the measure parameter in temperature sensors [54, 55].

Many papers reporting the enhancement of luminescence properties as a function of physical and chemical properties of rare-earth–activated glasses and crystals, or presenting some potential application as optical sensors, describe the luminescence spectroscopy as a suitable tool for quantitative characterization. In general, it is correct to state that the luminescence intensity of an indicator is dependent on the concentration of the respective chemical species or on the variation of the physical and chemical properties of the system [52, 56-58]. The disadvantage of intensity-based luminescence techniques, however, is that they suffer from variations in the intensity of the light sources, in the sensitivity of the detector, and in variation of the intensity of refractivity. A possibility of overcoming these problems is to use complementary results obtained by measuring the luminescence decay time of indicator cromophores and by the time-resolved fluorescence spectroscopy [23, 24, 59]. In the usual description of the photoluminescence process the intensity, I_{ij}, of an emission transition $i \to j$ is proportional to the spontaneous emission probability, A_{ij}, of the transition and the population density of the excited state, N_i: $I_{ij} \approx A_{ij}N_i$. The normalization to the total concentration N_T of optically active ions, gives $I_{ij}/N_T \approx A_{ij}n_i$, where $n_i = N_i/N_T$. The relative population, n_i, can be determined from rate equations of the specific investigated system. This requires the consideration of the processes involved in the population and relaxation of the energy levels of the luminescent ions [23,24]. In practical situations, the fluorescence experiments are performed under continuous or pulsed excitation. In the first case the system is considered in equilibrium, *i.e.* $dn_i/dt = 0$. By recording the fluorescence signal at a certain frequency, while varying the frequency of the exciting radiation, the so-called excitation spectrum is obtained. Such a spectrum can be correlated to the absorption spectrum of the system. The excitation spectrum is identical to the absorption spectrum if the ion decays rapidly from any higher excited state to the emitting state, which is known as Kasha's rule [60]. If the excitation spectrum shows deviation from the absorption spectrum, the measure is an indication of inhomogeneity of the spectral behaviour.

Measurements of the excitation spectrum are important in multisite systems, and can uncover the bands responsible for the energy storage and subsequent emission of the radiative energy. Important information has been obtained from excitation spectra in nanocomposite materials [58] and multicomponent glasses [61]. Under pulsed excitation, interesting information about the relaxation mechanisms can be obtained. In particular, the fluorescence decay time or lifetime of the emitting state can be determined. The intensity $I(t)$ of luminescence, resulting from exciting light whose intensity $K(t)$ varies with time t in an arbitrary way can be expressed by a Duhamel integral

$$I(t) = \int_0^\infty K(t-t')\phi(t')\mathrm{d}t', \tag{3.2.1}$$

where $\phi(t)$ is the decay function for pulsed excitation. This is generally valid under the condition that the number of excited molecules is small enough compared with the total number of molecules in the system and that the system does not undergo a permanent change such as photochemical reaction. For the particular case of a steady-state excitation turned off at $t = 0$, $K(t) = 1$ for $t < 0$ and $K(t) = 0$ for $t > 0$ in eq. (3.2.1), and the intensity of luminescence at a later time t is given by: $I(t) = \int_t^\infty \phi(t')\mathrm{d}t'$.

Two kinds of decay times can be considered. One is the mean duration of luminescence defined by $\tau_\mathrm{m} = \frac{\int_0^\infty t\phi(t)\mathrm{d}t}{\int_0^\infty \phi(t)\mathrm{d}t}$. The other is the $1/e$ decay time τ_e, or the time interval after which the intensity of luminescence has decreased by a factor of e from its value at $t = 0$. Thus, τ_e is defined as the root of the equation $\phi(\tau_e) = \phi(0)/e$. Of course, if the decay function is purely exponential, $\phi(t) = \phi(0)\exp[-\frac{t}{\tau}]$ and $\tau = \tau_\mathrm{m} = \tau_e$. Integration of eq. (3.2.1) with respect to t gives $\int_{-\infty}^\infty I(t) = \int_0^\infty \phi(t)\mathrm{d}t \int_{-\infty}^\infty K(t)\mathrm{d}t$. The physical meaning of this relation is that the total luminescence energy emitted in a sufficiently long time interval is proportional to the total energy of the exciting light in the same interval, and the proportional constant $\int_0^\infty \phi(t)\mathrm{d}t$ corresponds to the luminescence yield of the observed state.

The correct definition for the quantum yield Φ of a luminescent system is the ratio of the spontaneous emitted photons per unit time N_em divided by the total number of absorbed photons N_abs per unit time, $\Phi = N_\mathrm{em}/N_\mathrm{abs}$. The absolute measurement of the quantum yield is very difficult because of the geometry of the emission and the presence of re-absorption. It is usually measured in comparison with samples with known quantum yields or by using an integrating sphere. From eq. (3.1.7) the number N_abs of absorbed photons of energy $\eta\omega$ is given by $N_\mathrm{abs} = N_\mathrm{T}\frac{P_\mathrm{abs}}{\eta\omega} = N_\mathrm{T}\sigma_\mathrm{abs}(\omega)\frac{I}{\eta\omega}$. By considering negligible the temperature dependence of the absorption cross-section [26,27] $N_\mathrm{em} = N_\mathrm{abs}\frac{\tau_\mathrm{meas}}{\tau_\mathrm{r}}$. Therefore, the quantum efficiency of a luminescent state characterized by a radiative lifetime τ_r and an experimentally measured lifetime τ_meas is given by $\Phi = \tau_\mathrm{meas}/\tau_\mathrm{r}$.

In general, the fluorescence decay function $\phi(t)$ is not exponential, as discussed before, due to local environment inhomogeneities. In the most general case, when the relaxation refers to a number of locally active channels varying throughout the system, the stretched exponential or Kohlrausch model [62,63] is used: $\phi(t) = \phi(0)[\exp[\frac{t}{\tau}]^\beta]$, where $0 < \beta < 1$. In the simplest case, where the distance between the fluorophore and the interaction sites is homogeneously distributed, the total decay function is calculated by the integration of the differential equation that describes the time evolution of the excited state and the

summing-up over all sites,

$$\phi(t) = \phi(0) \exp\left[-\frac{(1+c)t}{\tau} - a\left(\frac{t}{\tau}\right)^{1/2}\right], \tag{3.2.2}$$

where a is the interaction parameter between cromophore and matrix, and c is the quenching parameter, which depends on the concentration of the chemical species to detect. If two different components of $\phi(t)$ can be observed, then it is possible write the relation $\phi(t) = A\phi_A(t) + B\phi_B(t)$, where A and B describe the relative amounts of the two chemical species or local environments present in the system. It has to be noted that the difference between the decay times corresponding to the forms A and B must be significant, a factor 100 being a good value of reference. The non-exponential decay function reported above has been used by Kitamura *et al.* [64] to describe the energy migration among organic molecules, which were dispersed in amorphous silica glass, and the energy trapping by the organic molecules aggregated in the glass. As mentioned before, in particular cases where the decay curves exhibit two well-separated components $\phi(t)$, with lifetimes τ_1 and τ_2, it is possible to determine the amounts of the two kinds of ions involved in the process. This is of particular interest in Er^{3+}-activated glasses, in order to have an assessment of the fraction of ions in the $^4I_{13/2}$ state that are available for optical amplification [65]. The fluorescence decay function $\phi(t)$ is then described by a sum of two exponentials, $\phi(t) = A_1 \exp[-\frac{t}{\tau_1}] + A_2 \exp[-\frac{t}{\tau_2}]$. The number N_i ($i = 1, 2$) of ions which will decay with the lifetime τ_i is obtained by integration of the previous equation, so that $N = N_1 + N_2 = A_1\tau_1 + A_2\tau_2$. Using this approximation, Zampedri *et al.* have shown that in $(100 - x)SiO_2$-$(x)TiO_2$-$1ErO_{3/2}$ planar waveguides prepared by the sol-gel route, for $x \leqslant 12$, about 65% of the Er^{3+} ions in the $^4I_{13/2}$ metastable state decay exponentially with a lifetime of about 8 ms [65].

3˙3. *Raman and Brillouin scattering for optical-glasses characterization.* – Raman and Brillouin spectroscopies are powerful non-destructive tools for the structural characterization of materials, in particular of multicomponent glass systems. These techniques, however, are widely used for the study of inorganic, organic and hybrid materials, both in massive, fibre and planar waveguide format. In the case of optically guiding structures, the exciting laser light is usually coupled to the system by butt coupling or through a grating, or by prism coupling, as shown in fig. 4. The theoretical and experimental background of Raman spectroscopy has been illustrated in several articles and scientific books. A clear and exhaustive presentation, corroborated by a rich bibliography, was given by Demtröder [25]. A recent review, concerning Raman and Brillouin spectroscopy for study of sol-gel–derived glasses, was given by Montagna [66]. The Raman effect is an inelastic scattering event in which a photon of energy $\eta\omega_i$ is destroyed and a scattered photon of energy $\eta\omega_{s/as} = \eta\omega_i \mu E$ is created. $E = |E_f - E_i|$ is the energy of the phonon created or destroyed in the processes necessary to move the system from the initial state E_i to the final state E_f. When the energy of the scattered photon is lower than the energy of the incident photon, we have a normal Stokes process; if the contrary occurs, we have an anti-Stokes process. The basic schema and the energy relations for Raman scattering are shown in fig. 6. The application of Raman spectroscopy as both qualitative and quantitative analytical detector is only limited by its inherent lack of sensitivity: approximately 1 in 10^7 photons is scattered at an optical frequency different from that of source excitation [67].

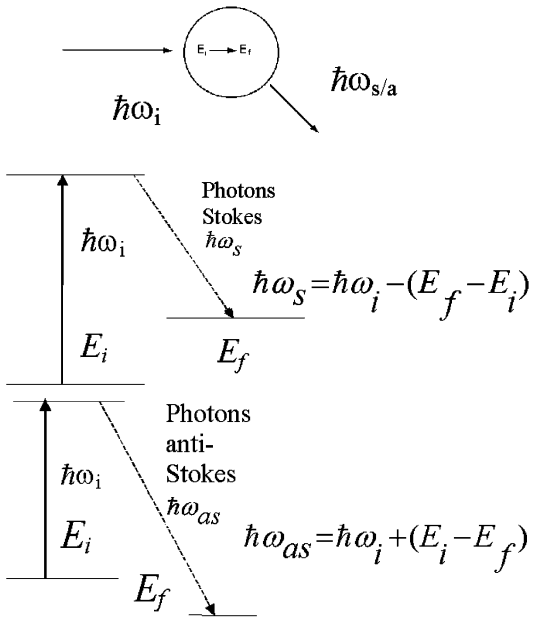

Fig. 6. – Basic schema and energy relations for Raman scattering.

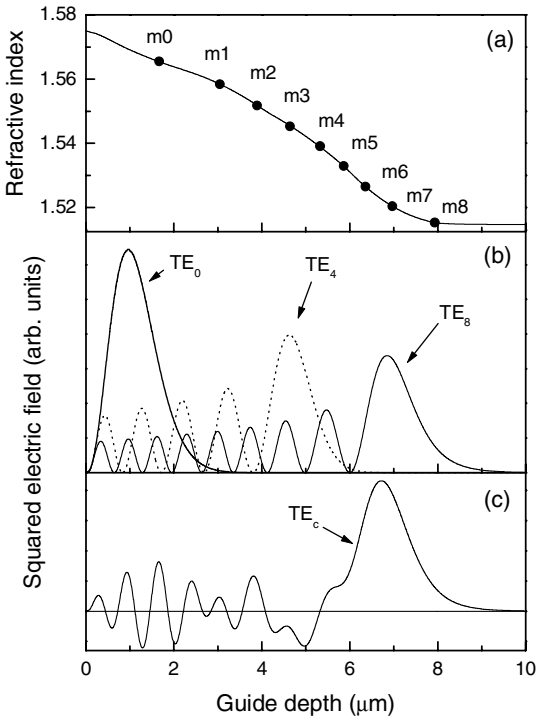

Fig. 7. – (a) Refractive index profile at 543.5 nm; (b) squared electric-field profiles for $m = 0$, 4, 8, respectively; (c) linear combination TE_c of the squared electric fields.

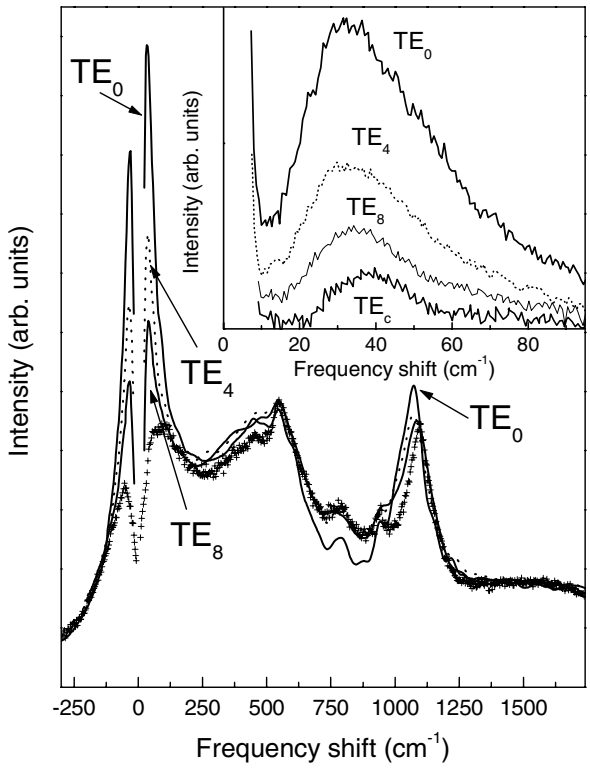

Fig. 8. – Raman spectra of the substrate (+) and of the $m = 0$ (solid line), 4 (dot line), and 8 (solid line) TE modes. In the inset, the low-frequency part of the spectra. TE_c labels the spectrum obtained by the linear combination used to produce the squared electric profile of fig. 7(c).

The combination of dielectric waveguides and Raman spectroscopy, however, leads to a useful and sensitive method to analyse thin active layers present on top of the waveguides. In the case of a graded-index waveguide, it is also possible to perform Raman and luminescence depth-selective measurements [68]. Referring to this case, fig. 7 shows (a) the refractive index profile, together with (b) the profile of the squared electric field for some transverse electric (TE) modes, in a graded-index waveguide obtained by silver exchange on a soda-lime glass substrate. The TE_0 mode is confined in a layer of about $2\,\mu$m thickness, but the depth reached by the light increases with the mode number m. The TE_m selectivity is evident in fig. 8, where the optical modes of the Raman spectrum show a dependence on composition, and in particular on the concentration of the diffused silver. In fact, the peak at about $1000\,\mathrm{cm}^{-1}$ shifts to lower frequencies and increases in intensity when m decreases, *i.e.* when the Ag content increases. Moreover, the low-frequency peak, which is better visible in the low-frequency region of the Raman spectrum shown in the inset of fig. 8, shifts towards higher frequencies as m increases. This observation is confirmed by the particular linear combination of the Raman spectra indicated by TE_c, which is drawn in fig. 7(c). It shows how the linear combination TE_c of the nine modes results in a squared electric field that is maximum in the region around $7\,\mu$m. The corresponding Raman spectrum (in the inset of fig. 8) shows that the

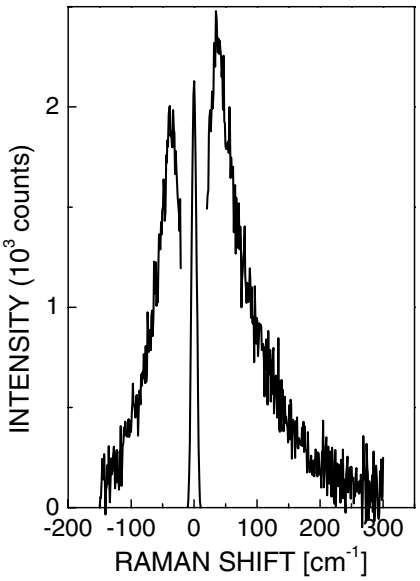

Fig. 9. – Room temperature VV spectrum of a silver exchanged silica waveguide, obtained by waveguide excitation of the TE_0, mode at $\lambda = 514.5\,\text{nm}$. Adapted from [30].

maximum of the peak is shifted towards higher frequencies. This indicates that in the selected region around $7\,\mu$m, where the Ag concentration is quite low, small metal clusters are present. This has been confirmed by transmission electron microscopy measurements on similar samples: the mean-size dimension and the size dispersion decrease as the Ag concentration decreases. The only assumption made in this analysis was that the spectra measured for excitation in one of the TE modes were the sums of contributions from different depths, with weights given by the local value of the squared electric field. This should be a good assumption for the luminescence and also for Raman, which is a coherent scattering effect, but with a coherence length in the glass on the nanometer scale, namely, much shorter than the film thickness [68].

Waveguide Raman spectroscopy is also a powerful tool for determining the particle size in a nanocomposite system [30]. After the first works of E. Duval *et al.* on spinel nanocrystals in cordierite glasses [70], low-frequency Raman scattering from symmetric and quadrupolar acoustic vibrations of the spherical clusters has become a reliable method to determine the size of nanoparticles. In fact, the frequency of all acoustic modes scales as the inverse of the linear dimension of the particle, which can indeed be deduced from the peak energy in the Raman spectra. For spherical particles, the only Raman active modes are the symmetric and quadrupolar spheroidal modes [71, 72]. The two modes give polarized and depolarized Raman spectra, respectively. The surface mode, namely the lowest frequency mode in the sequence with a given angular symmetry, has much higher Raman activity than the inner modes.

The Raman spectrum of a free spherical particle is expected to involve the contribution of only one discrete vibration. For silver particles, for example, the quadrupolar surface vibration is expected to dominate the Raman spectrum, all other modes having intensity

of few percent [72]. For a free sphere, the frequency of this mode is given by

$$\omega_2 = \frac{2\pi A v_t}{d}\,, \tag{3.3.1}$$

where v_t is the mean transverse sound velocity ($\sim 1660\,\mathrm{m/s}$ for Ag), d is the diameter of the particle, A is a constant of the order of unity ($A = 0.85$ for Ag). This equation can be used to obtain the size distribution of the nanoparticles from the shape of the Raman peak. To do this, two important effects must be considered. First, a free sphere has a discrete set of vibrational modes, but when the sphere is embedded in an elastic medium, the discrete set broadens into a continuum (homogeneous broadening). Second, the Raman activity is strongly dependent on the size of the particles $I(\omega, R) \approx R^3 \approx \omega^{-3}$. In the presence of an important size distribution (inhomogeneous broadening), the maximum of the experimental peak does not correspond to the maximum of the distribution, but to particles with size bigger than the mean size. Both these effects produce a shift of the peak towards lower frequencies. This gives rise to an overestimation of the particle size if equation $\omega_2 = 2\pi A v_t/d$ is applied taking exactly the value of ω_2 corresponding to the peak. The correct mean size and the size distribution are obtained by deconvoluting the homogeneous line shape and by considering the frequency (size) dependence of the Raman coupling coefficient. Figure 9 shows the excited spectrum of an Ag-containing film waveguide obtained by Ag^+-Na^+ ion-exchange in soda-lime glass [69]. The spectrum was taken in VV polarization by exciting the TE_0 mode of the guide with about 10 mW of the 514.5 nm line of the Ar^+ laser. By using eq. (3.3.1) with $\omega_2 = 36\,\mathrm{cm}^{-1}$ (the value of the peak energy), one would obtain $d = 1.3\,\mathrm{nm}$. By considering the low-frequency shift of the peak, produced by the homogeneous and inhomogeneous broadening, a mean size of about 1 nm is estimated, with an upper limit of the broad size distribution of about 1.5 nm, in good agreement with the TEM data.

The low-frequency Raman scattering technique was successfully employed in a number of material cases, such as the study of nucleation of Ga_2O_3 nanocrystals in the K_2O-Ga_2O_3-SiO_2 glass system [73], oxy-fluoride ultra-transparent glass ceramics [74], silica-tiania waveguides [75], and silicon quantum dots in glass matrix [76].

Raman spectroscopy is also very useful in structural characterization of glassy systems, because it allows one to get detailed information about the network intermingling and densification degree. As an example, Raman spectra of xerogels show the presence of OH^- groups, which strongly influence the matrix stability and are detrimental for the quantum yield of rare-earth–activated glasses; several studies and detailed discussions can be found in refs. [66, 77]. Let us discuss here the analysis of the densification process of an Er_2O_3-SiO_2 monolithic xerogel [78]. Curves (a) to (g) in fig. 10 show the VV polarized Raman spectra of the silica xerogels containing 0, 1000, 2000, 5000, 10000, 20000 and 40000 Er/Si ppm, respectively. In order to achieve densification, all the samples were annealed with a thermal treatment in air at 950 °C for 120 hours with a heating rate of 0.1 °C/min. Raman spectra allowed us to put in evidence that not all the xerogels exhibited the same degree of densification. Three spectral regions are shown in fig. 10: (I) anti-Stokes and Stokes low-frequency region, (II) the region between 250 and 1500 cm^{-1} and (III) the region between 3500 and 3800 cm^{-1}. Figure 10(I) clearly shows the so-called Boson peak, which is a characteristic of the glassy state and is a strong indication of complete densification of the sample. In the sample containing 2000 Er/Si ppm (curve (c) in fig. 10(I)), for instance, the Boson peak is not present. The Raman spectra of fig. 10(II) show bands at 430, 800, 1100 and 1190 cm^{-1}, assigned to the silica network. The band

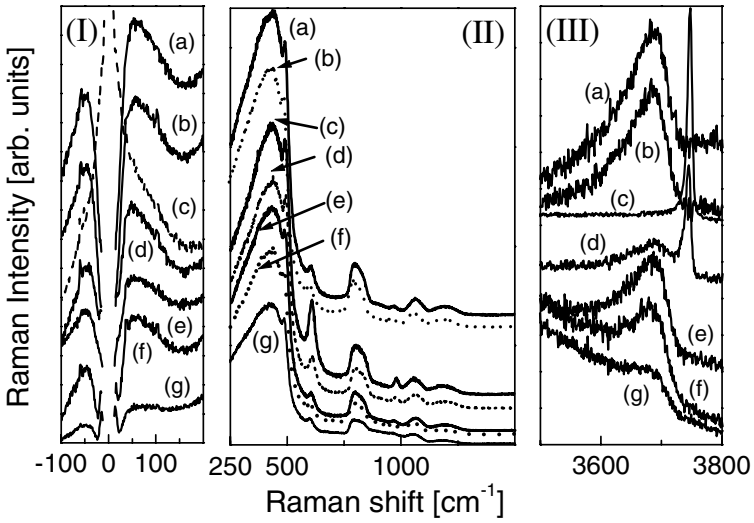

Fig. 10. – Room temperature Raman spectra of the 0 (a), 1000 (b), 2000 (c), 5000 (d), 10000 (e), 20000 (f) and 40000 (g) Er/Si ppm doped Er_2O_3-SiO_2 xerogel annealed at 950 °C for 120 h. (I) and (III) excitation at 488 nm; (II) excitation at 458 nm [78].

at 960 cm^{-1} is due to the Si-OH vibration. The defects bands D1 and D2, located at 490 and 610 cm^{-1}, respectively, are more intense for the samples doped with 2000 and 5000 Er/Si ppm than for the others samples. Finally, the Raman spectra in fig. 10(III) show two bands centred at about 3670 and 3750 cm^{-1}: the latter one is present only for the 2000 and 5000 Er/Si ppm doped samples. This band is assigned to the O-H stretching vibration of free silanol groups on the surface of a porous structure [79]. It is much sharper than the bands of physical and chemical water, because the SiOH groups at the pore surface are only weakly perturbed by site-sensitive interactions. The broad band centred at 3670 cm^{-1} is the fingerprint of OH groups in the densified silica structure [80]. In conclusion, the Raman spectra undoubtedly indicate that complete densification is achieved after annealing at 950 °C in all samples, except in those activated by 2000 and 5000 Er/Si ppm.

As to another important diagnostic tool, namely Brillouin scattering in solids, an exhaustive discussion is reported in ref. [81]. The Brillouin scattering results from the interaction between incident light beam and thermally generated acoustic waves, and can be successfully employed in determining the elastic and photo-elastic constants of glasses.

In this application area, Shen *et al.* recently showed that rare-earth modifier ions play a very important role in the structure of glasses, due to their higher coordination number and large atomic size [82]. Looking at Brillouin scattering spectra of Eu^{3+}- and Pr^{3+}-doped soda alumina silicate glasses, their photo-elastic constants were determined by comparing the relative Brillouin scattering intensity and frequencies of these glasses with those of fused quartz. The results indicated that the glass structure becomes more rigid, and the bonding structure becomes more ionic, when the rare-earth concentration is increased. The authors showed that the elastic constants, Young's modulus and bulk modulus of Eu^{3+}-activated glasses were higher than those of Pr^{3+}-activated glasses.

In order to perform and analyse Brillouin scattering experiments in planar waveguide

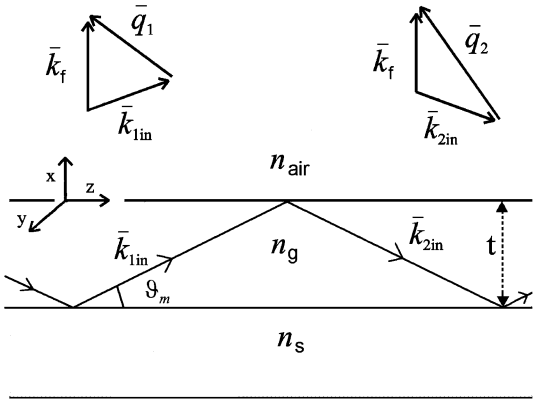

Fig. 11. – Wave propagation in the planar waveguide: $\bar{q}_1$ and $\bar{q}_2$ are the exchanged wave vectors of the scattered light in the zigzag paths. In TE modes, the electric field is along the y-direction, the light propagates along the z-direction, and x is perpendicular to the plane of the waveguide in the direction of the scattered wave. n_s and n_g stand for the refractive indices of the substrate and waveguide, respectively [66].

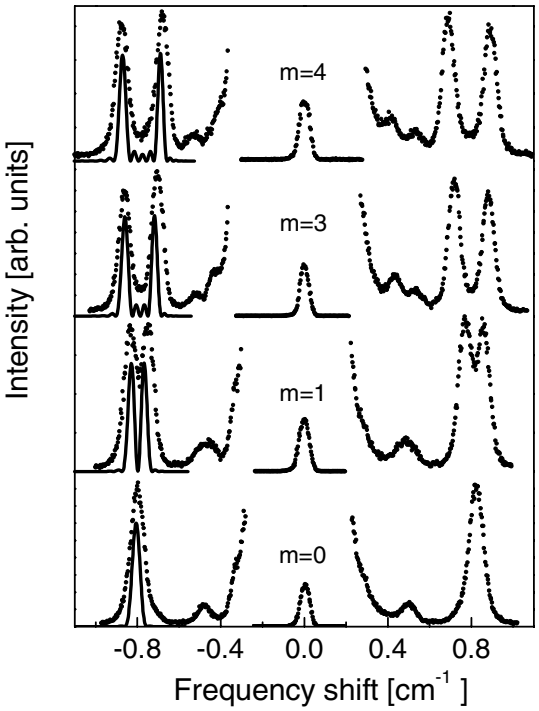

Fig. 12. – Brillouin spectra (dotted line) of a silica-titania thick planar waveguide obtained by excitation in different TE_m modes and detection perpendicular to the plane of the guide. The continuous curves (solid line) in the anti-Stokes part are the spectra calculated by using a numerical model, which considers the spatial distribution of the modal exciting field [83].

configuration, an *ad hoc* model has to be adopted [66, 83-85]. The wave propagation in a guiding film is shown in fig. 11; Brillouin scattering from acoustic vibration depends on the exchanged q vector of the scattered photon, and is a coherent process, which involves the whole illuminated region. In a homogeneous waveguide the light propagates along a zigzag path so that at a fixed angle of detection two values of q are sampled. Since the two q values change with the mode index, Brillouin spectra present doublets at different frequencies for different excitation modes. Under these conditions the Brillouin scattering intensity intensity I_{BS} is given by

$$I(\vec{q}_1, \vec{q}_2, \omega) \propto \frac{T}{\omega^2} \left| \int q_1 e^{i(\vec{k}_{\mathrm{p}} - \vec{q}_1)\vec{r}} + e^{i\gamma} q_2 e^{i(\vec{k}_{\mathrm{p}} - \vec{q}_2)\vec{r}} \mathrm{d}\vec{r} \right|^2 , \tag{3.3.2}$$

where T is the temperature, $\omega = v_{\mathrm{L,T}}\, k_{\mathrm{p}}$, $v_{\mathrm{L,T}}$ is the longitudinal, transverse sound velocity, $\vec{k}_{\mathrm{p}}$ the wave vector of the phonons which scatter the light, and γ is the relative phase of the zigzag fields in the m mode of the guide. The linear dependence of I_{BS} on T is always present in I_{BS} equation. The Brillouin spectrum of a glass waveguide, however, shows four peaks in the Stokes and four in the anti-Stokes spectrum, two peaks being due to longitudinal phonons and the other two to transverse phonons. The energy separation between the couple of peaks increases with the mode index.

This model neglects the contribution to the scattering coming from the evanescent field in the substrate, and considers the waveguide as a homogeneous film with constant refractive index. A single fit parameter, *i.e.* the longitudinal sound velocity, is used to calculate the $m+1$ spectra obtained by exciting the different modes of the waveguide. As an example, fig. 12 shows the Brillouin spectrum of a silica-titania waveguide obtained by exciting different TE modes with an argon laser at 514.5 nm and collecting the diffused light in a direction nearly perpendicular to the waveguide plane. Two longitudinal and two transverse peaks are observed, whose splitting increases with the mode index m (except for the $m = 0$ excitation, where no splitting is observed). The spectra calculated by using a numerical model, which considers the spatial distribution of the exciting field in the mode, are reported on the anti-Stokes spectrum of the longitudinal phonons. Using this approach, the longitudinal sound velocity in planar waveguides was determined with high accuracy, and it was demonstrated that waveguide Brillouin spectroscopy, coupled with waveguide Raman spectroscopy, is a powerful tool for structural characterization of guiding structures [83, 85].

4. – Absorption and emission cross-section measurement

A widely used method for relating the absorption and emission spectra of rare-earth–activated glasses and crystals, and in particular for Er^{3+} ions, is the McCumber theory [86], with the procedure developed by Miniscalco and Quimby [87]. An attractive aspect of McCumber's theory is that its validity is based on general assumptions. One of these, which is accepted by the scientific community, is that there is a thermal distribution of population among the individual Stark level components of each Stark manifold. Another assumption is that the energy width of each individual Stark level is small compared with $k_{\mathrm{B}}T$, where k_{B} is the Boltzmann constant and T is the absolute temperature. Detailed discussion about the validity of the McCumber model is reported in [88-90]. Anyway, the McCumber model has been successfully applied to the modelling of the performance of traditional and innovative bulk glasses as well as of a wide variety of fibre- and waveguide-based lasers and amplifiers.

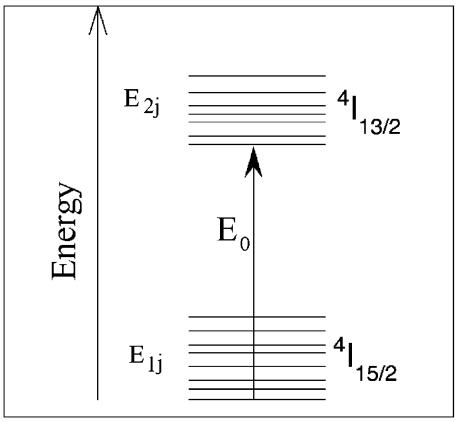

Fig. 13. – Diagram of the Stark manifold of the two lowest-energy levels of Er^{3+} ion.

In this section the basics of the model will be presented, and the Er^{3+}-activated glasses will be used as examples of absorption and emission cross-section measurements [42, 91]. Figure 13 shows a representative energy level diagram for the two Stark manifolds in an Er^{3+}-activated glass. The ground state $^4I_{15/2}$ is a manifold of eight sublevels of energy E_{1j}, and the $^4I_{13/2}$ excited state is a manifold of seven sublevels of energy E_{2j}. The McCumber relation states that the absorption cross-section $\sigma_{\rm a}(\nu)$ and the emission cross-section $\sigma_{\rm e}(\nu)$ between these manifolds are related by

$$\sigma_{\rm e}(\nu) = \sigma_{\rm a}(\nu) \exp[(\varepsilon - h\nu)/k_{\rm B}T], \tag{4.1}$$

where ν is the frequency of the photon of energy $h\nu$ involved in the process, and ε is the temperature-dependent excitation energy. The physical interpretation of ε is as the

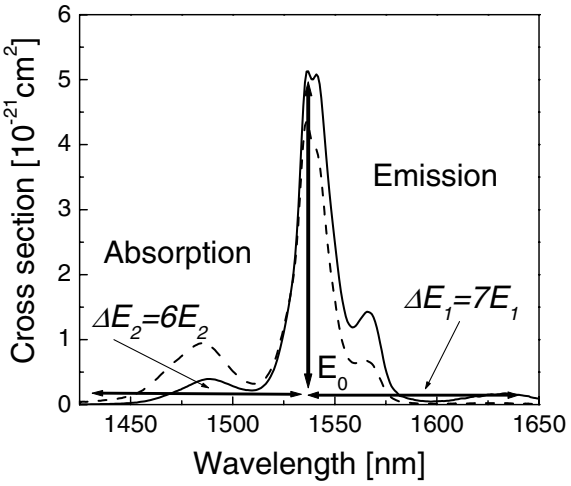

Fig. 14. – Absorption and emission cross-section spectra of Er^{3+} ion at 1.5 μm of a silicate glass, which illustrate the McCumber-Miniscalco-Quimby procedure. Adapted from [42].

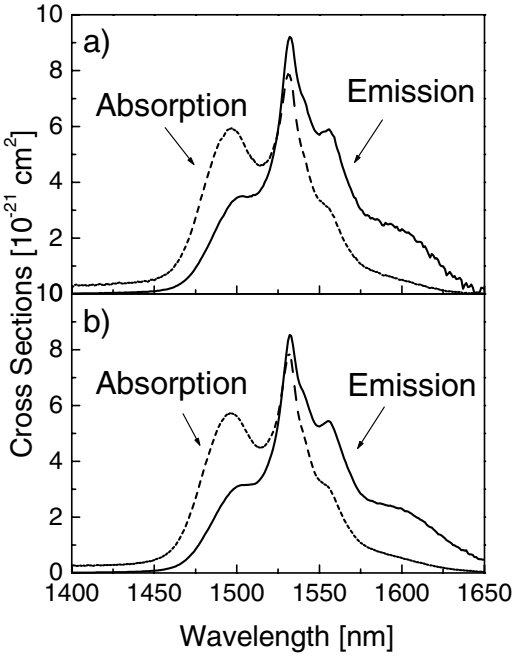

Fig. 15. – Absorption and emission cross-sections of Er^{3+} ion at 1.5 μm in the tellurite glasses of molar composition (a) 75 TeO_2: 12 ZnO: 10 Na_2O: 2 PbO: 1 Er_2O_3 and (b) 75 TeO_2: 12 ZnO: 10 Na_2O: 2 GeO_2: 1 Er_2O_3 [91].

net free energy required to excite one Er^{3+} ion from the $^4I_{15/2}$ to the $^4I_{13/2}$ state at temperature T:

$$\exp\left[\frac{\varepsilon}{k_{\mathrm{B}}T}\right] = \frac{\sum_{j=1}^{8}\exp\left[-\frac{E_{1j}}{k_{\mathrm{B}}T}\right]}{\sum_{j=1}^{7}\exp\left[-\frac{E_{2j}}{k_{\mathrm{B}}T}\right]}\exp\left[\frac{E_0}{k_{\mathrm{B}}T}\right] = C\exp\left[\frac{E_0}{k_{\mathrm{B}}T}\right], \tag{4.2}$$

where $E_0 = E_{21} - E_{11}$ is the difference in energy between the lowest energy levels of the two Stark manifolds as shown in fig. 13. Since the manifold widths exceed $k_{\mathrm{B}}T$, the absorption and emission spectra are offset from each other, the absorption to higher frequency and the emission to lower frequency, as shown in fig. 14. Equation (4.1) states that absorption and emission cross-sections are equal only at the crossing frequency $\nu_{\mathrm{c}} = \varepsilon/h$ when $C = 1$ and $\varepsilon = E_0$ (see eq. (4.2)).

Another parameter often used in the literature is the ratio R of peak emission to peak absorption cross-sections. The relation between R and C strongly depends on the spectral shape and it is not simple. In fact, as it may be observed in fig. 14, in general C and R differ, so that crossing is not perfect. Figure 14 and eq. (4.1) indicate that at frequencies higher than ν_{c}, the emission cross-section is smaller than the absorption cross-section, and vice versa for $\nu < \nu_{\mathrm{c}}$.

The inherent difficulty of the strict application of the McCumber method is that the

sublevel energies of Er^{3+} are difficult to be accurately known and, in principle, they must be measured for every host [92, 93]. The procedure developed by several authors [87-90] does not require the knowledge of these energies. The McCumber-Miniscalco-Quimby model first assumes a simplified electronic structure in which the Stark levels for a given manifold are equally spaced: $E_{1j} = (j-1)E_1$ and $E_{2J} = (j-1)E_2$ for the $^4I_{15/2}$ and for the $^4I_{13/2}$ manifolds, respectively. This reduces the number of parameters in eq. (4.2) from 14 to 3: i) the energy E_1 separating the Stark components of the ground state; ii) the energy E_2 separating the Stark components of the first excited state; iii) the energy E_0 which determines the separation between the two states. In this framework, the energy E_0 is chosen as the average of the absorption and emission peaks (see fig. 14). The second approximation consists in putting the energy spread of the $^4I_{15/2}$ state, $\Delta(^4I_{15/2}) = 7E_1$, at the 95% low-energy half-width of the room temperature emission spectrum, since the peak has already been identified with the transition between the lowest component of the two manifolds. This procedure provides an approximate value of E_1. In a similar way, the 95% high-energy half-width of the absorption spectrum is adopted for the width of the excited state manifold, $\Delta(^4I_{13/2}) = 6E_2$, thus providing an approximate value for E_2. Figure 14 well describes the approximation introduced by the McCumber-Miniscalco-Quimby model. By using these values of E_1 and E_2 in eq. (4.2), one can get an approximate expression for the constant C:

$$C = \frac{\sum_{j=1}^{8} \exp\left[-(j-1)\frac{E_1}{k_B T}\right]}{\sum_{j=1}^{7} \exp\left[-(j-1)\frac{E_2}{k_B T}\right]} . \tag{4.3}$$

Figure 15 shows the calculated absorption and emission cross-sections for two tellurite glasses [91]: the resulting values are very similar to those calculated for other tellurite systems. Their very high values are due to the high values of the refractive index, since the stimulated emission cross-section of rare-earth ions increases with the refractive index as $(n^2+2)^2/n$ for electric-dipole transitions, and as n for magnetic-dipole transitions [94].

The effective bandwidth $\Delta\lambda$, related to the emission cross-section, is defined by $\Delta\lambda = \int \sigma_e(\lambda)\mathrm{d}\lambda/\sigma_P(\lambda)$, where $\sigma_P(\lambda)$ is the peak value of the emission cross-section [94, 95]. This value, together with those of absorption and emission cross-sections, is especially important for the amplifiers in the wavelength-division-multiplexing (WDM) network systems [4,5]. Table II lists the cross-sections and the bandwidth concerning the $^4I_{13/2} \leftrightarrow {}^4I_{15/2}$ transition of Er^{3+} ion in some glass hosts. It is evident from table II that the parameters $\Delta\lambda$, σ_a, and σ_e strongly depend on the glass composition, which play a crucial role on the whole spectroscopic properties through the modification of the local environment of the rare-earth ions [96].

Finally, the internal gain coefficient g at wavelength λ can be estimated by means of the formula $g(\lambda) = \sigma_e(\lambda)N_2 - \sigma_a(\lambda)N_1$, where $\sigma_a(\lambda)$ and $\sigma_e(\lambda)$ are the absorption and stimulated emission cross-sections at wavelength λ, and N_1 and N_2 are the density of ions in the ground and excited state, respectively ($N_1+N_2 = N$, N being the density of erbium ions) [4]. Referring to the values reported in fig. 15, in the case of total inversion ($N_2 = N$) at 1532 nm, Rolli *et al.* obtain a gain coefficient of 4.06 and 3.78 cm^{-1}, respectively, for two tellurite samples activated by different Er^{3+} content, namely $N = 4.405 \times 10^{20}\,\mathrm{cm}^{-3}$ and $N = 4.426 \times 10^{20}\,\mathrm{cm}^{-3}$ [91]. Benoit *et al.* in silicate glasses estimated to obtain

TABLE II. – *Effective bandwidth ($\Delta\lambda$), absorption (σ_a) and emission (σ_e) cross-sections for the $^4I_{13/2} \leftrightarrow {}^4I_{15/2}$ transition of Er^{3+} at the indicated wavelength for some glass hosts.*

Host matrix	λ (nm)	σ_a (10^{-21} cm^2)	σ_e (10^{-21} cm^2)	$\Delta\lambda$ (nm)	Ref.
Al-P silica	1531	6.6	5.7	43	[87]
Silicate L22	1536	5.8	7.3	20	[87]
Silicate (Baccarat)	1537	4.3	5.1	18	[42]
Fluorophosphate L11	1533	7	7	27–43	[87]
Fluorophosphate L14	1531	5	5	63	[87]
GeO_2-SiO_2	1530	7.9	6.7	25	[69]
Al_2O_3-SiO_2	1530	5.1	4.4	55	[69]
GeO_2-Al_2O_3-SiO_2	1530	4.7	4.4		[69]
Tellurite	1532	7.9	8.2	66	[91]

an internal gain coefficient of about 2.0 dB at 1537 nm. Figure 16 shows the internal gain curves *vs.* the wavelength for a silicate glass, at different values of the fractional upper-state population N_2/N [42]. The change in the upper-state population strongly modifies the internal gain coefficient of the glass in the full 1460–1580 nm spectral range. Indeed, for low values of the population inversion, the glass is like an absorber of the light for the shorter wavelengths, while it amplifies the longer wavelengths.

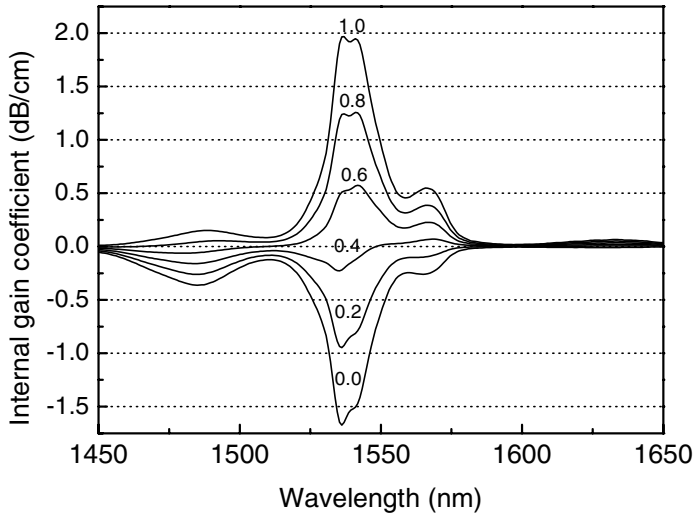

Fig. 16. – Calculated internal gain coefficient *vs.* wavelength in a silicate glass for different values of the fractional upper-state population N_2/N indicated on the graph for each curve [42].

5. – Quantum efficiency evaluation

As mentioned in the previous section, the measured lifetime (τ_{meas}) must be compared with the radiative lifetime, τ_{rad}, to obtain the quantum efficiency η defined by their ratio: $\eta = \tau_{\text{meas}}/\tau_{\text{rad}}$. The value of τ_{rad} can be calculated via different theoretical approaches and numerical analysis. First, if the emission cross-section is known, on the basis of McCumber-Miniscalco-Quimby model the radiative lifetime can be calculated from the following equation: $1/\tau_{\text{rad}} = \frac{8\pi n^2}{c^2}\int \nu^2 \sigma_{\text{em}}(\nu)\mathrm{d}\nu$. The second approach consists in a model based on Einstein's relation for the emission probability of a two-levels system for which g_1 and g_2 are the degeneracy of the lower state 1 and the upper state 2, respectively [97]. For such a degenerate system one condition has to be satisfied: either the sublevels making up each level are all equally populated, or the transition strengths between the sublevels are all equal. Taking into account only the decay pathway via the spontaneous emission for the $2 \to 1$ transition, and denoting A_{21} as the corresponding transition rate (Einstein A coefficient), the radiative lifetime of the upper state 2 is given by

$$\frac{1}{\tau_{21}} = A_{21} = \frac{8\pi}{\lambda^2}\frac{g_1}{g_2}\int \sigma_{12}(\nu)\mathrm{d}\nu, \tag{5.1}$$

where $\lambda = \lambda_0/n$ is the wavelength of the transition in the medium (λ_0 is the wavelength in vacuum, and n the refractive index), and $\sigma_{12}(\nu)$ is the absorption cross-section at the frequency ν [21, 91].

The two above-mentioned methods are of particular interest for the estimation of ${}^4I_{13/2}$ radiative quantum yield. A more general approach in determining the radiative lifetime is based on the so-called Judd-Ofelt theory, which yields an assessment of the oscillator strength characterizing the intensity of a transition between two ${}^{2S+1}L_J$ multiplets within the $4f^n$ configuration of a rare-earth ion [13, 14]. In the framework of the Judd-Ofelt theory, the theoretical oscillator strengths $P^{\text{ed}}_{\text{cal}}$ are expressed as a sum of transition matrix elements, involving intensity parameters Ω_q, with $q = 2, 4, 6$, which depend on the host matrix:

$$P^{\text{ed}}_{\text{cal}}(J, J') = \frac{8\pi^2 mc}{3h\lambda(2J+1)}\frac{\left(n^2+2\right)^2}{9n}\sum_{q=2,4,6}\Omega_q \left\langle aSL, J \left\| U^{(q)} \right\| a'S'L', J' \right\rangle^2, \tag{5.2}$$

where λ is the mean wavelength of the transition and n is the refractive index. Because the transition matrix elements $\langle \| U^{(q)} \| \rangle$ are essentially the same from host to host, the values calculated by Morrison are widely employed [98, 99]. Using the set of free-ion parameters obtained by Carnall in aqueous solution [100], Morrison computed the reduced matrix elements between all of the intermediate-coupled wave functions representing the multiplets of the electronic configuration $4f^n$ of the free ion. The intensity parameters, called Judd-Ofelt parameters, are then obtained by the chi-square method [101]. This method minimises the relative differences between the theoretical oscillator strength and the experimental one, $P^{\text{ed}}_{\text{exp}}$, measured in the absorption spectrum:

$$P^{\text{ed}}_{\text{exp}} + P^{\text{md}}_{\text{cal}} = \frac{mc^2}{\pi e^2}\frac{2303}{N_{\text{A}}}\int_{\text{band}} \varepsilon(\nu)\mathrm{d}\nu, \tag{5.3}$$

TABLE III. – *Intensity parameters Ω_q (in units of $10^{-20}\,\mathrm{cm}^2$) in the* 77.29 SiO_2: 11.86 K_2O: 10.37 PbO: 0.48 Sb_2O_3 *glass activated by* 0.2 mol% Er^{3+} *and* 0.5 mol% Er^{3+}. *The calculated radiative lifetime and the estimated quantum efficiency of the* $Er^{3+}\,{}^4I_{13/2}$ *metastable level, obtained using the three different methods described in sect.* **5**, *are also reported* [42].

Er^{3+} content	Ω_2	Ω_4	Ω_6	r.m.s.	τ_{rad} (ms) Quantum efficiency		
(mol%)					Judd-Ofelt	Einstein	McCumber
0.2	3.36	0.75	0.17	1.38×10^{-7}	17.8 ms 79.8%	18.9 ms 75.1%	20.1 ms 70.6%
0.5	3.19	0.56	0.16	6.5×10^{-8}	18.4 ms 62.5%	17.9 ms 64.2%	19.3 ms 59.6%

where $\varepsilon(\nu)$ is the molar absorptivity, ν is the wave number and N_{A} is Avogadro's number. Each value of the oscillator strength is weighed by its own uncertainty. These uncertainties have been evaluated by considering the reliability of the absorption bands integration including the baseline subtraction. As an indicative example, table III reports the obtained Judd-Ofelt (J-O) parameters in the case of a silicate glass [42], together with the root mean square (r.m.s.) deviations of the oscillator strengths, calculated as

$$\text{r.m.s.} = \left[\frac{1}{N-3}\sum_{i=1}^{N}\left(P^{\mathrm{ed}}_{\mathrm{exp}}(i) - P^{\mathrm{ed}}_{\mathrm{cal}}(i)\right)\right]^{1/2}, \tag{5.4}$$

where N is the number of fitted bands. After obtaining the J-O parameters, the total spontaneous emission probabilities and the radiative lifetimes τ_{r} of the most important excited states of the rare-earth ions can be estimated. The electric-dipole contributions have been computed as follows [102]:

$$A_{\mathrm{ed}}(\Psi J;\Psi' J') = \frac{64\pi^4 e^2}{3h\lambda^3(2J+1)}\chi_{\mathrm{ed}}\sum_{q=2,4,6}\Omega_q\left\langle aSL, J\left\|U^{(q)}\right\|a'S'L', J'\right\rangle^2, \tag{5.5}$$

where Ω_q is the set of J-O parameters determined from the chi-square minimisation, λ is the mean wavelength of the transition, $\chi_{\mathrm{ed}} = \frac{n(n^2+2)^2}{9}$ is the local field correction, and $\langle\|U^{(q)}\|\rangle$ are the reduced matrix elements tabulated by Morrison [98, 99]. The magnetic-dipole contributions only depend on the magnetic-dipole operator and are given by

$$A_{\mathrm{md}}(\Psi J;\Psi' J') = \frac{4\pi^2 e^2 h}{3\lambda^3 m^2 c^2(2J+1)}\chi_{\mathrm{md}}\left\langle aSL, J\left\|(L+2S)^{(1)}\right\|a'S'L', J'\right\rangle^2, \tag{5.6}$$

where $\chi_{\mathrm{md}} = n^3$ is the local field correction and $\langle\|(L+2S)^{(1)}\|\rangle$ are the magnetic dipole matrix elements also tabulated by Morrison in the intermediate-coupled wave functions set. The radiative lifetime of an excited state i is then governed by $\tau_{\mathrm{rad}}(i) = (\sum_j A(i,j))^{-1}$, where $A(i,j) = A_{\mathrm{ed}}(i,j) + A_{\mathrm{md}}(i,j)$ and the summation is over all the terminal states j. Finally, the emission branching ratios are given by $\beta_{ij} = A(i,j)\tau_{\mathrm{rad}}(i)$.

When two emitting states are separated by a small energy gap, the thermalization phenomenon must be taken into account. For instance, $^2H_{11/2}$, $^4S_{3/2}$ and $^4F_{5/2}$, $^4F_{3/2}$ pairs of emitting levels of the Er^{3+} ion are in thermal equilibrium and are commonly treated by considering the Boltzmann distribution.

All these methods allowing one to estimate the radiative lifetime lead to an indirect measure of the quantum efficiency. In a recent paper, the Er^{3+} $^4I_{13/2}$ radiative lifetime was calculated applying the three methods described above for a same silicate sample; the resulting values were in good agreement between them, despite the different procedures employed from one method to the other, but the McCumber method provided the longest lifetimes and therefore the lowest quantum efficiencies [42]. It is obvious that the different results are related to the approximation used in each method. Both in Einstein relationships between absorption and emissions processes and in Judd-Ofelt model the approximation holds that all Stark levels of the ground J state are equally populated. It is the so-called "natural excitation" of Condon and Shortley [103]. Both in Judd-Ofelt and two-levels models the generally used value for the degeneration factor g_2/g_1 is $(2J_2 + 1)/(2J_1 + 1)$. This issue has been exhaustively discussed by Auzel in a recent paper [104], where it is underlined that the results for quantum efficiency calculations of the $^4I_{13/2}$ to $^4I_{15/2}$ transition of several Er^{3+}-doped glasses show errors up to 50% for a maximum Stark splitting of about 260 cm^{-1} at 300 K, when the value of the degeneracy factor $g_2/g_1 = (2J_2+1)/(2J_1+1) = 14/16 = 0.87$ is used. It turns out that the Einstein and Judd-Ofelt approach overestimate the quantum efficiency. The correction proposed by Auzel started from the assumption that the $^4I_{13/2}$ to $^4I_{15/2}$ transition of Er^{3+} could be experimentally described by four transitions between two unresolved levels separated by their maximum Stark splittings: 180 and 260 cm^{-1}. Taking into account their respective Boltzmann population distribution at 300 K and the experimental intensities for the four groups of their relative matrix elements, the effective degeneracy factor g_2/g_1 was determined to be $\cong 1.36$ instead of 0.87, for $\Delta E/k_B T \cong 1.25$. Very recently, such source of error has been considered for the Yb case as well, where quantum efficiencies much larger than one had been obtained. Instead of $g_2/g_1 = 6/8 = 0.75$, it was found that, at 300 K, the effective degeneracy factor was 1.18 [105]. This corresponds to an error of about 40% when the "natural excitation" approximation was used [104].

Finally, we mention an interesting method for the direct measurement of the quantum yield described by Auzel *et al.* [106]. They used a photoacustic cell, with a piezoelectric transducer in mechanical contact with the Er^{3+}-activated glass. The 980 nm line of a continuous wave Ti:Sapphire laser, resonant with the $^4I_{15/2} \rightarrow {}^4I_{11/2}$ transition of the Er^{3+} ion, was used as excitation source. The absorption and the photoacustic excitation spectra were simultaneously recorded. When the exciting beam is modulated at low frequency, typically few dozens of Hz, the quantum efficiency is proportional to the ratio of the photoacustic signal P to the absorbed excitation intensity A. In the case of Er^{3+} silicate glasses, the relation assumes the straightforward form $\frac{P}{A} = a + b\eta(1/\eta\omega)$, which is the equation for a straight line, where a and b are phenomenological constants. The slope of the line, normalized to its intercept *vs.* $1/\eta\omega$, gives directly the quantum efficiency.

More generally, photoacustic spectroscopy is well suited for the study of materials which are opaque or exhibit important scattering. An interesting discussion about this technique is reported in [107] and references therein.

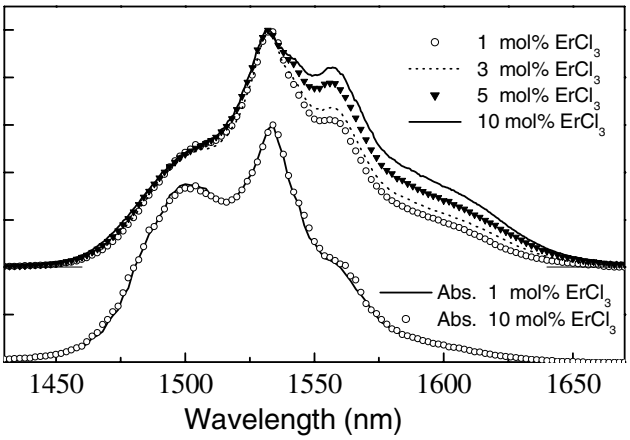

Fig. 17. – Normalized photoluminescence spectra of the ${}^4I_{13/2} \rightarrow {}^4I_{15/2}$ transition for tellurite glasses activated by different Er^{3+} content collected upon excitation at 980 nm in identical experimental conditions. Normalized absorption spectra of the ${}^4I_{13/2} \leftarrow {}^4I_{15/2}$ transition for 1 and 10 mol% Er^{3+}-activated glasses, are also reported. Adapted from [109].

6. – Radiation trapping, self-absorption and concentration-quenching phenomena

The previous discussion on the radiative lifetime measurements and the quantum efficiency, being connected to the goal of maximizing the fluorescence signal from an active optical glass, has been preliminary to the analysis of some important effects related to the rare-earth concentration in the glass itself.

As already noted in sects. **4** and **5**, the design of an erbium-doped broad-band amplifier first of all requires the measurement of the ${}^4I_{13/2} \rightarrow {}^4I_{15/2}$ effective transition bandwidth and lifetime. One of the phenomena affecting the accuracy of these measurements is self-absorption, which is defined as the reabsorption of luminescence by the analyte and interfering impurities in the excitation volume [108]. In a recent paper, Mattarelli *et al.* discussed the measurement of bandwidth and lifetime in the presence of self-absorption and indicated an experimental procedure to obtain their actual value [109]. A series of tellurite glasses, with nominal molar composition $60TeO_2$-20ZnO-$20ZnCl_2$-$x ErCl_3$, where $x = 1, 3, 5, 10$, were prepared. It was shown that, while the normalized absorption spectra in the region of the ${}^4I_{13/2} \rightarrow {}^4I_{15/2}$ transition of the Er^{3+} ion overlap one with the other, the normalized PL spectra exhibit a shape dependent on the Er^{3+} content (see fig. 17). It is noteworthy that the PL bandwidth $\Delta\lambda$, if calculated using the emission intensity $I(\lambda)$ instead of the emission cross-section as defined in sect. **4**, passes from 77 nm for the least doped sample ($x = 1$) up to 84 nm for the most doped one ($x = 10$) [109]. These results could lead to think that the growth of the Er^{3+} concentration is associated with the occupation by the active ions of more and more different microscopic environments, giving rise to a greater inhomogeneous broadening. This explanation, however, contrasts with the evidence of the absorption spectra, where the shape of the electronic transition does not change with the doping level (fig. 17). The observed broadening of the emission must, on the contrary, be ascribed to the self-absorption effect, that leads to overestimate the real emission bandwidth [110]. In fact, because of the overlap of the absorption and

emission spectra around the 1.53 μm peak, reabsorption around the peak wavelength is much more effective than that at other wavelengths. As a consequence, the measured emission intensity around the peak wavelength will be lower than its intrinsic value.

The influence of self-absorption on the luminescence shape can be described in first approximation, *i.e.* neglecting contributions from photons reflected or re-emitted after a first absorption, by the relationship

$$I_d(\lambda) = I_0(\lambda) \exp[-\alpha(\lambda) d], \tag{6.1}$$

where $I_d(\lambda)$ is the collected PL intensity for a penetration depth d, $I_0(\lambda)$ is the initially generated luminescence, and $\alpha(\lambda)$ is the absorption coefficient. Equation (6.1) means that it is also possible to reconstruct $I_0(\lambda)$ by multiplying the collected PL spectra by the correction factor $\exp[\alpha(\lambda)d]$. Mattarelli *et al.* have applied this procedure to PL measurements performed at different depths on the same sample, showing a remarkable agreement of the initially generated spectra $I_0(\lambda)$ [109]. In order to check the effectiveness of the procedure, PL spectra were collected from finely ground powders of each sample, with an average size of about 300–400 μm, where the deforming effect of self-absorption was strongly reduced. The PL spectra of the powders showed a shape independent of the Er^{3+} concentration, and they closely overlapped with the reconstructed spectra $I_0(\lambda)$. When the McCumber-Miniscalco-Quimby model is applied, the shape of the emission spectrum thus calculated reflects perfectly the spectra obtained with the above-shown method, giving the true value of the effective bandwidth, *i.e.* about 66 nm. These results confirm the goodness of the approximation in determining the self-absorption contribution from the absorption spectra.

Radiation trapping can also induce a misleading evaluation of the luminescence quantum efficiency, defined as the ratio of observed to radiative lifetime. Auzel *et al.* discussed the radiation trapping effect on the measured lifetime of several rare-earth ions in a single crystal [111]. When population inversion can be neglected, the measured lifetime in the trapping condition (τ_{tr}) is related to the intrinsic lifetime without trapping (τ_{intr}) by: $\tau_{\mathrm{tr}} = \tau_{\mathrm{intr}}(1 + \sigma N d)$, where σ is the transition cross-section, N is the ion doping concentration, and d is the average absorption length in the lifetime measurement experiment. It is evident that reabsorption can lead to a strong increase of the luminescence decay time and to a proportionally overestimated quantum efficiency. As an example, much higher τ_{tr} values (between 20 and 140% higher) were measured in tellurite massive glasses than in the corresponding powders, the latter being surely related to the intrinsic lifetime τ_{intr} [109].

The principle of radiation trapping can be demonstrated simply by coating a glass or crystal with a highly reflecting film and leaving apertures open for the entrance of excitation light and for observation of the luminescence decay. Noginov [112] experimentally demonstrated a sixfold increase for the Yb^{3+} lifetime in Yb^{3+}:BaY_2F_8 gold-coated crystal; in the uncoated sample the Yb^{3+} lifetime was 2.9 ms, to be compared with the lifetime of 18 ms measured in the gold-coated sample. Analogously, for the $^4I_{13/2}$ transition in Er^{3+}:BaY_2F_8, he measured 13 ms for the uncoated crystal and 31 ms for the gold-coated one. It is clear that radiation trapping enhances energy storage, energy transfer, and up conversion in rare-earth–activated materials. However, if the reabsorption effect is appropriately tailored, it can potentially decrease the threshold for compact continuous-wave pumped lasers.

Another effect that strongly decreases the efficiency of luminescent materials is the so-called concentration quenching. In the case of high rare-earth concentrations, the ions

are closer together, so that deleterious non-radiative energy exchanges between neighbouring ions can take place. The dissipative processes related to ion-ion interactions leading to concentration quenching in glasses have been the object of several studies, both theoretical and experimental, as shown by the number of publications dealing with the argument [87, 89, 113-118]. In the following we will refer only to the Er^{3+} ion, which is the most widely used in guided-wave amplifiers and lasers. When the erbium concentration increases, the average distance between neighbouring Er^{3+} ions simultaneously decreases and electric dipole-dipole interactions between the different Er^{3+} ions become more significant. Under this condition, processes which include energy migration and up-conversion can take place, lowering the fraction of excited Er^{3+} ions at a given pump power. As a consequence, a decrease of the luminescence lifetime of the metastable $^4I_{13/2}$ state as a function of increasing Er^{3+} concentration occurs, as described by the following empirical formula [87, 113]:

$$\tau_{\mathrm{meas}} = \frac{\tau_0}{1 + \left(\dfrac{\rho_{\mathrm{Er}}}{Q} \right)^p} , \tag{6.2}$$

where τ_{meas} is the observed luminescence lifetime, τ_0 the ideal luminescence lifetime in the limit of zero rare-earth concentration, ρ_{Er} the Er^{3+} ion concentration, Q the quenching concentration and p a phenomenological parameter characterizing the steepness of the corresponding quenching curve. It could be considered that p is determined by the mechanism of the energy transfer between the rare-earth ions [110]. In this framework, p is close to 2 when the electric dipole-dipole transition is the dominant energy-transfer mechanism between neighbouring Er^{3+} ions. When the effect of electric dipole- and quadrupole-quadrupole transitions cannot be neglected, p should be larger than 2. However, in order to avoid difficulties with the physical meaning of p, usually only Q is estimated from the fitting curve, as the concentration at which the lifetime becomes half of τ_0 (in fact, τ_{meas} is equal to $\tau_0/2$ when ρ_{Er} is equal to Q). The phenomenological equation (6.2) deserves some comments and, as a general rule, the Q parameter has to be considered in the light of complementary measurements, which may put in evidence other relaxation mechanisms. By definition, τ_0 is the value of the PL lifetime of the rare-earth ion in the material, in the limit of zero ion concentration, *i.e.* in the absence of any concentration quenching phenomena. Therefore, if the material has no multiphonon relaxation due to the matrix, which is approximately true for heavy-metal silicates, and if there are no residual OH^- species, then τ_0 should approximately coincide with the radiative lifetime τ_{rad}. But, if there a residual OH^- exists, even in the limit of zero rare-earth concentration, the τ_0 value should be less than the radiative lifetime. A detailed discussion with a numerical analysis about the validity of the concentration quenching relation is reported in [77].

Several researchers have noted that codoping with Al^{3+} is effective at dispersing rare-earth ions in silica gel and silicate glass matrices [96, 119-121]. A detailed interpretation of why and when rare-earth ion isolation occurs is still not well established [122]. A general point of view, however, is that rare-earth ions will be preferably partitioned by Al^{3+}, forming Al-O-RE bonds, rather than sitting together to form RE-O-RE bonds. Subsequently, the spacing among RE elements is larger in the alumina-doped silica host rather than in the non–alumina-containing host.

7. – Photonic band gap structures with glassy materials

Photonic crystals are structures characterized by a refractive index periodicity in space on a length scale comparable to the wavelength of interest, and, consequently, by a certain frequency range where light cannot propagate in any direction; this frequency range is known as the photonic band gap (PBG) [123-125]. It was predicted by Purcell [126] that an atom in a wavelength-size cavity can radiate much faster than in the free space. This effect was measured in a cavity formed by two parallel mirrors by Haroche *et al.* [127]. On the other hand, if its transition frequency falls within the photonic band gap, the atom cannot radiate away energy, and thus spontaneous emission can be completely inhibited [128]. Several configurations have been proposed to exploit the physical property that spontaneous-emission rate of rare-earth ions can be modified by the influence of the local optical environment. This effect has been demonstrated in one-dimensional systems such as Eu^{3+}-doped dielectric slab [129], Er^{3+}-activated Si/SiO_2 microcavity [130], Er^{3+} and dye-doped SiO_2 colloidal photonic crystals [131], and Pr^{3+}-doped Ta_2O_5/SiO_2 micro-resonators [132].

Photonic crystals are nowadays the key for the future technological development of planar optical circuits. To exploit the unique properties of photonic crystals it is important to develop new ways of making optically functional photonic crystals that integrate the self-assembly chemistry methods and the microfabrication techniques, with the aim of creating new photonic crystal devices and chips that are suitable for high-volume manufacturing processes.

Recently, it has been proved that the sol-gel technique represents a viable approach to the fabrication of PBG structures and, in particular, of rare earth-activated 1-D photonic crystals and microcavities [133-135]. A recent review of the origin and development of PBG materials and structures made by sol-gel processing since 1987, with emphasis on recent developments, can be found in [136]. Thin films of SiO_2 and TiO_2 were used to fabricate one-dimensional photonic crystal devices using the sol-gel method [137]. The microcavity resonator consisted of a TiO_2 Fabry-Perot cavity sandwiched between two SiO_2/TiO_2 mirrors of three bi-layers each. The resonance wavelength was at 1500 nm and the quality factor Q of the microcavity was 35.

As another example, Zampedri *et al.* reported a sol-gel–derived 1D cavity realized by an Eu^{3+}-activated dielectric layer placed between two distributed Bragg reflectors (DBR) [135]. These DBRs consisted of 7 alternated quarter-wave layers of TiO_2 and SiO_2. The active layer between the two DBRs consisted of a TiO_2 half-wave layer doped with 2 mol% of Eu^{3+}. The sample was deposited on vitreous silica substrate. The starting solution was $Ti(O\text{-}n\text{-}C_3H_7)_4$ and $Si(OC_2H_5)_4$, with molar ratio $H_2O/TiO_2 = 1$ and $H_2O/SiO_2 = 2$, employed for titania and silica layer preparation, respectively. The spinning deposition technique was used. After each spinning, the sample was dried at 200 °C for 1 minute on a hot-plate and then annealed at 1000 °C for about 90 s. Angle-dependent reflectance spectra and luminescence measurements were performed as described in [77]. For luminescence measurements with 1D microcavities, two angles must be controlled: the angle of excitation and the angle of collection of the luminescence. In fact, the excitation angle must be chosen so that the laser beam is not reflected by the DBRs, but good part of the excitation light could reach the active layer. The angle of collection of the luminescence is chosen in order to superimpose the cavity resonance to the rare-earth emission. For normal incidence, a stop band from about 510 nm to 800 nm, with maximum reflectance of 98%, was obtained, which is shown in fig. 18. The cavity resonance corresponded to the peak at 618 nm with a full width at half maximum

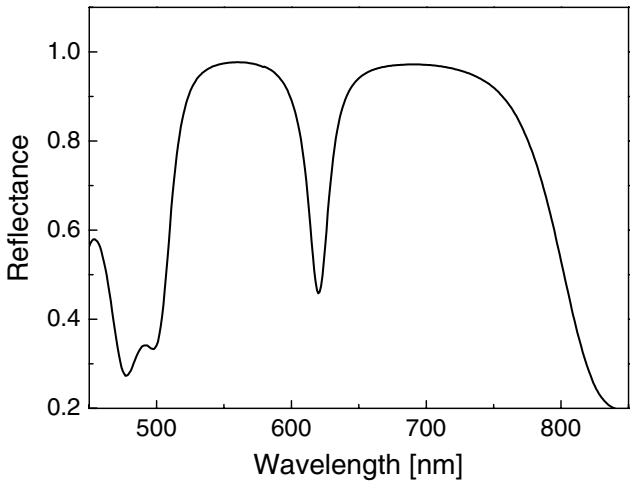

Fig. 18. – Normal incidence reflectance spectra of a sol-gel–fabricated Fabry-Perot microcavity, consisting of two mirrors of 7 alternated quarter wave layers of TiO_2 and SiO_2, plus a 2 mol% Eu^{3+}-activated TiO_2 half-wave defect layer [135].

(FWHM) of 12 nm. The cavity resonance depends on the detection angle; a quality factor $Q \cong 54$ was obtained in this case, with the reflectance measured for an incidence angle of 0°. The fabrication technique must be precisely controlled on the nanometric scale for fabrication of higher-Q microcavities; it is crucial, in particular, to avoid variations in the index and thickness of the different stacked layers.

Photoluminescence spectra of the microcavities show the interesting effect of luminescence enhancement. In the system described above [135], the luminescence, corresponding to the emission from ${}^5D_0$ state to the ${}^7F_J$ ($J = 2, 1$) levels of the Eu^{3+} ion, could be tuned by the PBG system in a wide frequency range, practically corresponding to the whole stop band. The maximum of the luminescence was detected at angles less than 10°. The luminescence line was modified both in intensity and bandwidth by the cavity. The FWHM value of about 12 nm for the ${}^5D_0 \rightarrow {}^7F_2$ emission had to be compared to the typical FWHM of about 25 nm observed in sol-gel–derived bulk glasses. When the doped layer, with a thickness of about 140 nm, was inserted into the cavity, an intense emission was detected. Oppositely, when the same layer was deposited on a silica substrate, a very low intensity, comparable to the noise, was observed. This enhancement of the luminescence was already demonstrated for instance by Vredenberg *et al.* [130] for a Si/SiO_2 cavity activated by Er^{3+} ions. The intensity enhancement occurs because at any particular wavelength the emission rate into a resonant cavity mode, which is highly directional, is increased, while in almost all other directions is reduced. This redistribution of emitted intensity is a well-known cavity effect and has been numerically analysed in detail for a complete set of cavity modes in planar dielectric microcavities [128]. It is evident that the possibility of controlling spontaneous emission makes these planar structures of great interest for fabrication of high emissive devices such as directive light-emitting diodes or low threshold microlasers.

It is evident that three-dimensional (3D) cavities would provide a really significant improvement in the light extraction; since, however, there exist serious difficulties in fabricating 3D PBG structures, in particular with deterministic defects, much effort is

being devoted to the less demanding 2D photonic crystal structures. Even these 2D structures, if associated with waveguide control in the third dimension, may actually provide an excellent overall 3D confinement. Rare-earth–doped glasses, however, do not lend themselves as very convenient materials for 2D or 3D PBG structures, due to the relatively low refractive index and consequent low index contrast. Despite of this limitation, some 2D fibre and waveguide devices have been proposed, by using microstructured glass technology [138].

8. – Rare-earth–doped glasses for lasers and amplifiers

Optical glasses are the corner stone in a huge number of technological applications. This is definitely true for laser systems. At the top of the scale, one can mention the National Ignition Facility (NIF) at the Lawrence Livermore National Laboratory, which has the goal to achieve controlled thermonuclear burn in the laboratory using laser light. The entire NIF project is expected to be completed in mid-2009, with ignition experiments beginning a year later [139]. NIF represents both the largest laser and the largest optical instrument ever built, requiring 7500 large optics and more than 30000 small optics. Optical materials, and in particular optical glasses, play a crucial role in NIF fabrication, where the neodymium-activated glass laser slab, operating at 1053 nm, is the hearth of the laser system.

Over almost 40 years there has been extensive research covering a large number of active ions in every known glass system. Neodymium, however, remains the primary RE element of interest for most commercial applications of glass lasers, and, more generally, of solid-state lasers. Only recently, a growing interest has been focused on erbium and ytterbium: the former ion is fundamental for applications in the optical telecommunications (but also has interest for eye-safe laser applications, such as in rangefinders), while the latter is useful as co-dopant of erbium (because of the energy-transfer effect that increases pumping efficiency at 980 nm) but is assuming larger and larger importance for the development of medium-to-high power fibre lasers. Ytterbium-doped silica fibres exhibit a broad-gain bandwidth, high optical conversion efficiency, and large saturation fluence. A cladding-pumped Yb-doped fibre laser with continuous-wave optical power of 1.36 kW at 1.1 μm, with 83% slope efficiency and near diffraction-limited beam quality, has been demonstrated [140]. By combining an assembly of highly reliable diode-pumped single Yb-fibre lasers, industrial systems with output up to 50 kW are also available [141].

Other rare-earth ions under investigation include samarium and holmium for visible emission, praseodymium for the 1.3 μm window, thulium and again holmium for longer near-infrared wavelengths. A summary of the main emission wavelengths of the most important RE ions is presented in table IV, where possible sensitising ions are indicated as well. Here we refer to a sensitising ion as the additional dopant that absorbs the pump radiation and transfers it to the lasing ion, thus increasing the overall pumping efficiency [142].

At the bottom of the scale of rare-earth–doped glass devices, at least for their miniaturised size, there are the integrated optical (IO) lasers and amplifiers: the following sub-section is devoted to an overview of IO amplifiers, which have gained much interest in the last years for their application in optical communication systems.

8˙1. *Integrated optical amplifiers.* – There are three major applications for optical amplifiers in modern optical networks; they can be used as power amplifier/boosters (placed

TABLE IV. – *Emission wavelengths of the main RE ions in glass.*

Dopant RE ion	Approximate emission wavelength(s) (μm)	Sensitising ion
Pr^{3+}	0.89 1.04 1.34	
Nd^{3+}	0.93 1.06 1.35	Cr^{3+}, Mn^{2+}, Ce^{3+}
Sm^{3+}	0.65	
Eu^{3+}	0.62	
Tb^{3+}	0.54	
Ho^{3+}	0.55 1.38 2.05	
Er^{3+}	1.30 1.54 1.72 2.75	Cr^{3+}, Yb^{3+}
Tm^{3+}	0.80 1.47 1.95 2.25	Er^{3+}, Yb^{3+}
Yb^{3+}	1.03	Nd^{3+}

directly after the laser diode transmitter), in-line amplifiers (repeaters), or preamplifiers (placed in front of the detector to enhance its sensitivity). The corresponding requirements may be different, especially in terms of input signal power handling, maximum optical gain, and signal-to-noise ratio (SNR). There are a few possible technological routes for implementing optical amplifiers: they include semiconductor optical amplifiers (SOAs) [143], erbium-doped fibre amplifiers (EDFAs) [144-146], and Raman optical amplifiers [147]. Hybrid configurations, such as Raman-assisted EDFAs, have also been extensively studied, because they show low noise figure [148].

EDFAs represent a mature technology, and they are routinely used in current telecommunication systems. Another application of optical amplifiers, especially in local access networks, has to do with the loss compensation of passive components (such as interleavers and $1 \times N$ splitters). In such a case, the final aim would be that of integrating active and passive devices on a single chip: for this reason, the integrated-optics (IO) format [149] is more appealing. IO amplifiers are being extensively investigated, and a few types of erbium-doped waveguide amplifiers (EDWAs) are already commercially available [150].

The goal of developing fibre systems operating over an ultra-wide band, covering the wavelengths between 1.3 and 2 μm, would require the use of different rare-earth (RE) elements and different glass matrices. The potential amplification bands in that wavelength region of some combinations of glasses and rare earths are indicated in table V. The energy levels are labelled according to the well-known Russel-Saunder multiplet notation $^{2S+1}L_J$, where S is the total spin quantum number, L is the total orbital angular-momentum quantum number, and J is the quantum number of the total momentum of that particular level or state ($J = L+S$) [151]. The choice of the glass matrix largely affects the amplifier's performance, and oxide glasses are not suitable hosts for exploiting the radiative transitions of Pr^{3+} in the 1260–1350 nm region, of Tm^{3+} in the 1460–1510 nm region, and of Ho^{3+} over 2000 nm.

So far, however, most of the research efforts have been focused on the use of Er^{3+} $^4I_{13/2} \rightarrow {}^4I_{15/2}$ transition in the 1500–1600 nm band, and for that purpose oxide glasses, and

TABLE V. – *Potential amplification bands in the near-infrared region of some RE ions in glass.*

Operating range (nm)	Dopant RE ion	Transition	Oxide host	Fluoride host
1260–1350	Pr^{3+}	$^1G_4 \rightarrow {}^3H_5$	−	+
1320–1400	Nd^{3+}	$^4F_{3/2} \rightarrow {}^4I_{13/2}$	+	+
1460–1510	Tm^{3+}	$^3F_4 \rightarrow {}^3H_4$	−	+
1500–1600	Er^{3+}	$^4I_{13/2} \rightarrow {}^4I_{15/2}$	+	+
1700–2015	Tm^{3+}	$^3H_4 \rightarrow {}^3H_6$	+	+
2040–2080	Ho^{3+}	$^5I_7 \rightarrow {}^5I_8$	−	+

especially silicates and phosphates, proved to be much more convenient than non-oxide glasses, due to their easier fabrication and processing, and to the higher chemical resistance. Thus, EDFAs and EDWAs based on oxide glasses remain at the moment the most viable solution to cover the C-band and its short side (S^+-band: 1450–1530 nm; or S-band: 1480–1520 nm) and long side (L-band: 1560–1610 nm).

Bulk rare-earth–doped glasses may be fabricated by conventional melt-quenching, sol-gel or CVD processes [20]. For integrated optics, several fabrication processes have been developed; material requirements are much more stringent than for optical fibres, due to the different manufacture technologies and to the much higher rare-earth concentration required in short-length planar devices. Even if in principle non-oxide glasses, such as fluorides and other halides, may possess better properties (*e.g.*, much lower phonon energy), so far the largest part of the experimental results—and all the available commercial amplifiers—have been obtained using silicates and phosphates glasses, mostly because of their greater chemical robustness and environmental stability.

The development of erbium-doped integrated optical amplifiers may follow three main manufacturing routes:

– local doping of a bulk glass or of a glass thin film with rare-earth ions by diffusion or ion-implantation; the process leads to a local increase of the refractive index, and therefore also produces a waveguide [152-155];

– fabrication of a rare-earth–doped bulk glass by conventional melting process or by sol-gel, and subsequent fabrication of the waveguide by diffusion processes (by ion-exchange, in particular) [156-163];

– deposition of a glass thin-film waveguide containing rare-earth ions by RF magnetron sputtering, chemical vapour deposition (CVD), electron-beam vapour deposition, flame hydrolysis deposition (FHD), or sol-gel processes [164-169].

A combination of two different technologies has also been demonstrated, such as sol-gel to deposit the Er-doped thin film and ion-exchange to define the channel waveguide [170], or flame hydrolysis deposition of the guiding layer and aerosol Er-doping [171], or ion-exchange in a glass to fabricate the waveguide and ion implantation to dope it with erbium [172]. Moreover, advances are being made in laser-based fabrication and patterning processes of glass structures, which include pulsed-laser-deposition [173-175], laser machining [176, 177], UV-laser and femtosecond-laser writing of channel waveguides in bulk glasses or in glassy thin-film [178-181].

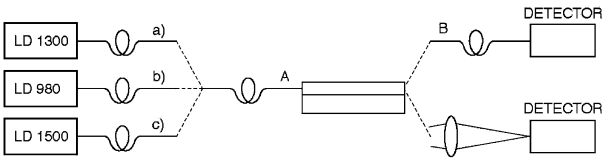

Fig. 19. – Experimental set-up used to measure the optical properties of an Er^{3+}-doped waveguide, pumped at 980 nm. Pigtailed laser diodes and output coupling configurations may be combined in different ways to perform specific measurements.

8˙2. *Optical and spectroscopic properties of* Er^{3+}*-doped waveguides*. – The goal of achieving a high optical gain in an Er^{3+}-doped glass can be reached only if the proper spectroscopic properties of the glass are combined with a low propagation loss waveguide. Thus, it is very important to optimize the RE doping level. Generally, at low Er^{3+}concentration, the lifetime of the metastable level is longer and quantum efficiency is higher, but obviously the total intensity of stimulated emission is lower, while at higher concentrations, fluorescence quenching may occur, due to ion clustering or ion-to-ion interaction. It is also important that absorption and emission spectra be wavelength-shifted one with respect to the other, so that the peaks of absorption and emission cross-sections are located at different wavelengths, in order to reduce re-absorption phenomena in the waveguide. This is possible because the $^4I_{13/2}$ Stark levels are non-uniformly populated, and the $^4I_{13/2} \rightarrow {}^4I_{15/2}$ transition may be shifted to a longer wavelength with respect to absorption.

For most of the amplifiers in the 1.53 μm band, the active doping includes ytterbium ions: ytterbium co-doping allows to transfer energy from excited Yb^{3+} ions to close Er^{3+} ions through a cooperative cross-relaxation process, thus significantly enhancing system absorption at 980 nm and making the pumping mechanism more efficient. The presence of Yb^{3+} ions may also be effective in reducing unwanted Er^{3+}-Er^{3+} ion energy transfer interactions by increasing the mean inter-atomic distance.

As to the waveguide itself, it is necessary to achieve minimal propagation losses, because they would affect, among other factors, the pump threshold, *i.e.* the power at which the material becomes transparent, the signal amplification being able to compensate for propagation and absorption losses.

The pumping scheme is also important, in order to actually excite the maximum number of erbium ions; in most cases the pump is a laser diode emitting at $\sim$ 980 nm wavelength, which corresponds to the peak of the absorption band due to the $^4I_{15/2} \rightarrow {}^4I_{11/2}$ transition. In order to achieve high pumping power, laser diode arrays are used, or a contradirectional scheme is employed, with two laser diodes injecting their power at the two ends of the fibre-EDWA-fibre system. Proper modelling is necessary, in order to select the optimal doping concentration and operational parameters [181-183].

The most important characteristic to indicate the performance of an EDWA is the net gain. Since it is not always clear, when reading some of the published papers, what kind of gain was actually measured, let us recall the definitions of gain and refer to fig. 19 to explain how a full characterization of an active waveguide may be performed, by using, in different configurations, the same basic devices, namely laser diodes, fibres, detectors, and the waveguide to be tested.

The *net optical gain*, also called *external gain*, can be measured as the ratio between the maximum intensity of the signal measured at the end of the output fibre (B) and

the signal intensity at the end of the input fibre (A), for a given value of the pump laser intensity. The intensity of the amplified spontaneous emission (ASE) should be subtracted from the output signal.

If, however, one wants to understand how that value of gain is obtained, it would be useful to perform a more detailed analysis, by measuring:

a) The insertion loss of the waveguide at a wavelength outside the absorption band of Er^{3+} ions, *e.g.*, at 1300 nm. This measurement can be done by comparing the intensity at the output of the delivery fibre (A) with that at the end of the collecting fibre (B). It gives an assessment of scattering losses; moreover, a correction due to the wavelength difference between 1.3 and 1.5 μm, according to Raleigh law $I_s = a\lambda^{-4}$, is possible.

b) The spontaneous emission intensity. This is measured by detecting the signal at the output of the collecting fibre (B) when the waveguide is pumped, *i.e.* when the delivery fibre (A) is carrying only the beam at 980 nm.

c) The coupling loss between the fibre and the channel waveguide may be evaluated by comparing the intensities detected when the light coming out from the channel is collected by a fibre or by a lens (usually, a microscope objective). Then, one can assume that the coupling loss is not significantly different for the input and the output coupling.

d) The absorption of erbium ions. This value is derived from the measure of the insertion loss at 1.5 μm, in the absence of the pump, by subtracting the coupling losses.

A preliminary and quick measure of the amplifier performance can be given by the *signal enhancement* (sometimes also referred to as *relative gain* or ON/OFF ratio), *i.e.* the ratio of output signals when the laser pump is on and off. This is not, however, a true optical gain, due to the effect of absorption of erbium ions, which is significant when the pump is off and becomes negligible when the ground state is depleted of electrons by the pump light. The *internal gain* may be obtained by subtracting from the signal enhancement the absorption due to erbium ions at 1.5 μm; by further subtracting the coupling losses, the value of the net optical gain G is finally obtained.

Table VI gives an idea of the state of the art in EDWAs, by presenting a few out of the many results published in the literature, with particular reference to devices fabricated in silicate and phosphate glasses. It has to be underlined that comparison of these results should be considered only qualitative, because it cannot be stated that measurement methods and units are used everywhere in a consistent way. For instance, in some cases the intensity of the pump signal is given as the optical power actually injected into the waveguide, while in other cases only the power available at the end of the input fibre is given.

Besides the gain, the other most important specification for an EDWA is its amplifier bandwidth, since the broad-band operation is critical for the use in DWDM systems. In fact, an EDWA has to simultaneously amplify many channels, with the best possible uniformity; as the gain is generally dependent on wavelength, each signal will experience different optical gain, with bad effect on the transmission bit-error rate (BER) and on the signal-to-noise ratio (SNR) differential among channels. Thus, not only the width of the emission band is important, but its shape as well, because it affects the uniformity of gain

TABLE VI. – *Characteristics and performance of a few* Er^{3+}*-doped integrated optical amplifiers, as reported in the literature.*

Material	Doping ion(s)		Fabrication technology	Max. Net Gain (dB/cm)	Pump power (mW)[a]	Ref.
	Er	Yb				
Aluminophosphosilicate	0.25 mol%	0.25 mol%	sol-gel	1.1	175	[168]
Borosilicate	3 wt% Er2O3	5 wt% Yb2O3	ion exchange	2.3	130	[157]
Doped BK7	1 wt% Er_2O_3	5 wt% Yb_2O_3	ion exchange	1.0	110	[186]
P-doped silica	0.55 wt%		FHD[c]	0.7	640	[164]
Phosphate	♦[b]	♦[b]	ion exchange	2.5	120	[159]
Phosphate	2 wt%	2 wt%	ion exchange	2.9	120	[186]
Soda-lime silicate	2.3×10^{20} ions/cm^3	3.8×10^{20} ions/cm^3	ion exchange	1.5	250	[160]
Soda-lime silicate	0.7×10^{20} ions/cm^3		sputtering	0.8	80	[165]

[a] If not indicated, pump wavelength is 980 nm. [b] Doping percentage not available. [c] FHD: flame hydrolisis deposition.

over the transmission channels. This fact has stimulated further research towards glass hosts providing wider photoluminescence bands and, more generally, a good compromise between the different operational characteristics, namely high gain, broad band and flat amplification.

A few examples of novel glass compositions are presented in the following subsections, which refer to recent activities carried out by the authors and collaborators, and concern silica-hafnia sol-gel films, aluminosilicate ion-exchangeable glasses and tellurite glasses.

8˙2.1. Sol-gel silica-hafnia films. Silica-based glasses offer solubility for rare-earth ions of about $6 \times 10^{20}\,cm^{-3}$, are transparent in the visible to near-infrared region, and are easily compatible with IO technology. Silica-hafnia thin films are known as stable optical coatings with high damage resistance at 1054 nm, and have been proposed for mirrors and polarizers for the National Ignition Facility. Thus, it was decided to test the structural and optical properties of Er^{3+}-doped optical waveguides made by silica-hafnia; for that purpose, by using the sol-gel process, several films of composition $(100-x)SiO_2$ - $xHfO_2$ (x = 10, 20, 30, 40) were produced and tested. For each composition, two films were grown, containing 0.01 and 0.3 mol% Er^{3+} ions, respectively [184].

All the films were deposited on cleaned pure-silica substrates by dip coating. After each layer's deposition, the sample was annealed in air for 50 s at 900 °C. After a 10-dip

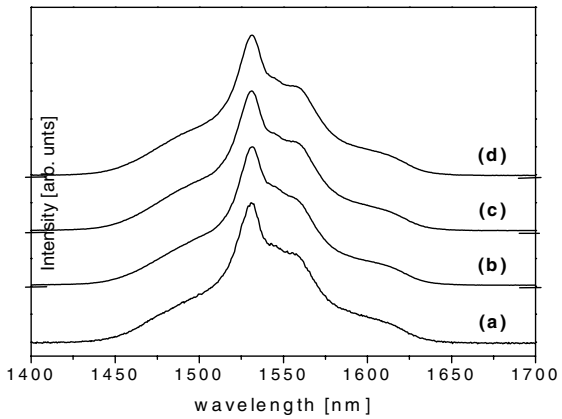

Fig. 20. – Photoluminescence spectra relative to the ${}^4I_{13/2} \rightarrow {}^4I_{15/2}$ transition of the Er^{3+} ions for the (a) SH40, (b) SH30, (c) SH20, and (d) SH10 waveguides, obtained upon excitation at 514.5 nm.

cycle, the film was heated for 2 min at 900 °C. Finally, the waveguides were subject to a further annealing at 900 °C, whose duration was different for each waveguide; for instance, for the samples containing 0.3 mol% Er^{3+}, the annealing time was varying from 30 hours ($x = 10$) down to 5 minutes ($x = 40$). As the refractive index was changing with each composition, the thickness of each film was chosen so to have a single mode of propagation (one TE and one TM mode) supported at 633 nm. More details on the fabrication process are available in previous papers [184,185]. Measurements of propagation losses were done in various samples, giving an average value of about 0.9 dB/cm at 632.8 nm.

Photoluminescence (PL) measurements in the region of the ${}^4I_{13/2} \rightarrow {}^4I_{15/2}$ transition and decay curves from the ${}^4I_{13/2}$ level were made in guided-wave configuration, using prism coupling and either the 980 nm line of a Ti:sapphire laser or the 514.5 nm line of an argon laser as excitation source. The PL spectra relative to the ${}^4I_{13/2} \rightarrow {}^4I_{15/2}$ transition of the Er^{3+} ions for all the waveguides exhibited a main emission peak at 1.53 μm and a broad spectral width of about 50 ± 2 nm. Figure 20 shows the emission spectra of the samples doped with 0.3 mol% Er^{3+} for excitation at 514.5 nm; the shape and the bandwidth of these spectra, however, did not change with the excitation wavelength, indicating that site selection was negligible. The similarity of PL spectra for all waveguides seems to indicate that a small inhomogeneous broadening is present, independently of HfO_2 content.

The measured lifetime of the ${}^4I_{13/2}$ metastable state decreases with the increasing of the HfO_2 molar concentration, from a maximum of 8.5 ms when the ratio SiO_2/HfO_2 is 90:10 and Er^{3+} concentration 0.01 mol%, to a minimum of 5.8 ms when the ratio increases to 60:40 and erbium concentration is 0.3% mol. By considering that in completely densified silicate glasses the multiphonon decay does not significantly affect the ${}^4I_{13/2}$ level lifetime, we can assume that the lifetimes measured at 0.01 mol% Er^{3+} doping level are very close to the radiative ones. Under this hypothesis, we can estimate that quantum efficiency even in the samples doped with 0.3 mol% of erbium is always higher than 84%.

8˙2.2. Soda-lime-alumino-silicate (SLAS) glasses. Soda-lime-silicate glasses are quite widely used in optics, and in integrated optics as well. As an example, a net optical gain of 1.5 dB/cm was demonstrated in a glass of this type, co-doped with Er^{3+} and

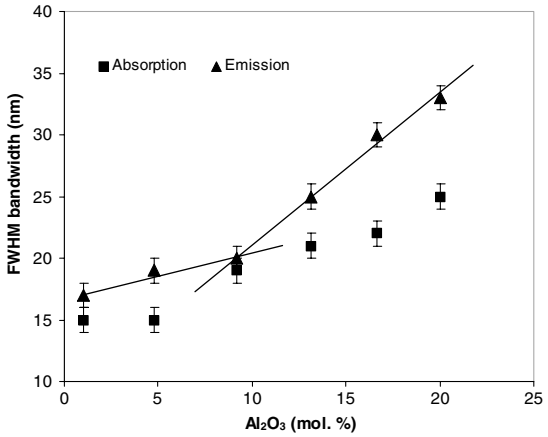

Fig. 21. – Absorption and emission bandwidths of SLAS samples as a function of Al_2O_3 concentration. The lines are traced only as a guide to the eye.

Yb^{3+} [160]. One disadvantage of this kind of glass, however, was represented by the narrow fluorescence bandwidth, the full-width half-maximum (FWHM) value being around 17 nm. On the other hand, it was known that the introduction of aluminium in a silicate glass may lead to increase the emission bandwidth [187]. Thus, it was decided to try to improve the characteristics of the original glass by adding different quantities of aluminium oxide (up to about 20 mol%) and by investigating their effect on glass optical properties, in particular on the emission bandwidth around 1.5 μm.

The new glasses were prepared by conventional melting process and had a basic composition of the type Na_2O-CaO-Al_2O_3-SiO_2, with small percentages of P_2O_5 and K_2O. Melting occurred in an electrically heated furnace within Pt crucibles, following the same heating cycle: from 20 to 1000 °C at 10 °C/min, with a 24 h soaking time at 1000 °C, from 1000 to 1550 °C at 20 °C/min and finally 1 hour of soaking time at the maximum temperature of 1550 °C. Eventually, the melt was quenched in a graphite mould to obtain small pieces of glass having a bar form; each bar was then cut to 1 mm thickness and optically polished on both faces.

Planar optical waveguides were produced by using the $Ag^+ \Leftrightarrow Na^+$ exchange process in a dilute $AgNO_3$ solution ($AgNO_3 : NaNO_3 = 0.5 : 99.5$ mol%) at 325 °C. Both the fluorescence spectra of Er^{3+} and the lifetime τ of the $^4I_{13/2}$ level were detected using a 976 nm laser diode as excitation source. Further details on fabrication and characterization of these glasses are available elsewhere [188]. An interesting result was that the bandwidth almost doubled when passing from 1 to 20 mol% of alumina. The broadening of both the absorption and the fluorescence spectrum is also shown in fig. 21, where one can notice that the slope of increase of the emission bandwidth changes significantly from the region where the alumina content is lower than 9 mol% to the region where the content is equal or higher than 13 mol%. Correspondingly, an abrupt change in the physical (density) and optical (bulk refractive index) properties of the glass was observed as well (fig. 22) [188]. These facts suggest that the behaviour of this class of glasses has a drastic change when the concentration of aluminium ions becomes larger than that of sodium ions. A possible explanation refers to the different effect that the aluminium oxide has on the silica network, as glass modifier and as glass former, respectively. In

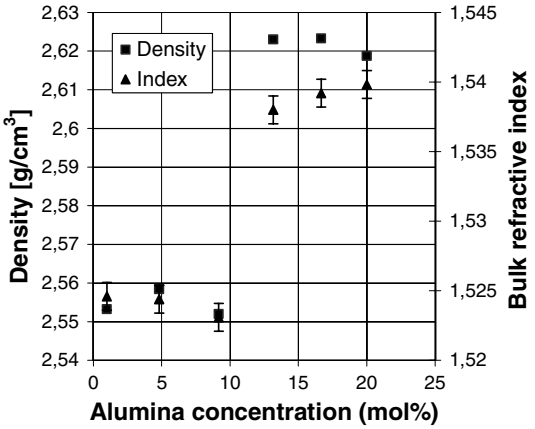

Fig. 22. – Density and bulk refractive index of the six glass samples as a function of alumina content. The error on the measurement of density is lower than $0.0004\,\mathrm{g/cm^3}$ and therefore in the plot the error bar would be smaller than the symbol used.

particular, in the network modifier case (samples with Al_2O_3 concentration lower than 10 mol%), the aluminium ions contribute to disrupting the silica structure and producing non-bridging Al-O groups, which can coordinate the Er^{3+} ions, so reducing the Er-Er interaction and increasing the lifetime of the metastable $^4I_{13/2}$ level. A further increase of aluminium oxide, on the contrary, reduces the non-bridging oxygen ions to form the Al-O-Si bridging oxygen.

The radiative lifetimes were calculated using Judd-Ofelt analysis; for all the samples, the quantum efficiency $\eta = \tau_{\mathrm{meas}}/\tau_{\mathrm{rad}}$ is larger than 55%. Quantum efficiency near 75% is estimated for the sample having high Al_2O_3 concentration (16.67 mol%): this sample, therefore, exhibiting high η and broad emission bandwidth, can represent a glass with high potential for an EDWA.

8˙2.3. Tellurite glass waveguides. In the recent years, a growing attention has been paid to TeO_2-based Er^{3+}-doped glasses, which exhibit large stimulated emission cross-sections, broad emission bandwidth, wide infrared transmittance (up to $6\,\mu$m), and low phonon energy. Modelling has shown that the tellurite-glass host material can offer two kinds of advantage for the fabrication of high-gain integrated optical amplifiers: i) Er^{3+}-doped tellurite waveguides exhibit higher signal gains than Er^{3+}-doped silica waveguides, and ii) the broader bandwidth that Er^{3+} exhibits in tellurites, coupled to its higher emission cross-section coefficient, reduces the deleterious gain peaking effect and therefore makes it easier to reach the goal of a gain-flattened optical amplifier [182].

We studied two families of tellurite glasses, one including tungsten and the other one including zinc [189]. The composition of the samples we synthesized and characterized is summarized in table VII. Samples S1 and S2, which pertain to the zinc-tellurite set, also contain 2 mol% of Pb and Ge, respectively. Their respective bandwidths were 63 nm and 66 nm, and their lifetimes resulted to be 3.3 ± 0.2 and 2.9 ± 0.2 ms. The corresponding calculated quantum efficiencies resulted to be 94% and 83%. Similar values of lifetimes and quantum efficiencies were found for the other samples.

Near-infrared to visible upconversion upon CW excitation at 976 nm has been observed in all the zinc tellurite samples, even at low excitation powers (≈ 1 mW) indicating

TABLE VII. – *Molar composition of investigated erbium-doped tellurite glasses* [91, 162].

Sample	TeO_2	Na_2O	ZnO	WO_3	PbO	GeO_2	Er_2O_3
V1	60	15		25			0.05
V2	60	15		25			0.5
V3	60	15		25			1
V4	60	15		25			1.5
V5	60	15		25			2
S1	75	10	12		2		1
S2	75	10	12			2	1
N1	80	10	9				1
N2	80	9	9				2

that these glasses also have potential as efficient hosts for upconversion generation.

Planar waveguides were successfully obtained in both types of glass, by using Ag^+-Na^+ ion-exchange; eutectic mixtures of $AgNO_3$, KNO_3 and $NaNO_3$ salts were used to keep the process temperature lower than the transition temperature of the glasses. Characterization of the diffusion process shows that the diffusion depth clearly decreases with increasing Er^{3+} concentration. Tungsten-tellurite glasses appear to be more convenient for IO device fabrication because of the shorter exchange times necessary to produce a single-mode waveguide at 1.5 μm [162]. This is due to the higher exchange temperature (330 °C instead of 280 °C), made possible by the higher transition temperature of this glass (T_g = 356 °C) with respect to zinc-tellurite glass (T_g = 290 °C). Both types of glasses, on the whole, exhibit modal and spectroscopic characteristics that, even with their pros and cons, make them quite promising for the development of broad-band integrated optical amplifiers.

9. – Microspherical lasers

In dielectric spheres light can be guided through high-Q whispering-gallery-modes (WGMs) with a unique combination of strong temporal and spatial confinement of light. Glass microspheres are therefore of interest for a large number of applications as cavity quantum electrodynamics, nonlinear optics, photonics, and chemical or biological sensing [190]. After the early works of Garret *et al.* [191] and the works on Morphology Dependent Resonances (MDRs) and lasing effects in droplets during the 1980's [192], rare-earth–doped glass microsphere lasers recently became a subject of numerous studies and have been demonstrated as potentially compact laser sources [193, 194]. Figure 23 shows the up-converted green light propagating at the surface of an erbium-doped glass microsphere, upon excitation by a laser diode emitting at 980 nm through a half-taper fibre (not visible in the photo) for evanescent-field coupling. The microsphere is glued to the end of an optical fibre for easy handling.

A microspherical laser based on Er^{3+}/Yb^{3+} co-doped phosphate glass, optically pumped at 1480 nm, with emission at around 1550 nm, was demonstrated [195]. Interesting effects on the laser emission were noticed, due to the interaction between the WGM modes of the glass sphere and an external metal mirror. Johnson [196] presented a theoretical treatment of the MDRs of a dielectric sphere in close proximity to a surface of infinite conductivity and calculated the changes of the locations and widths of the

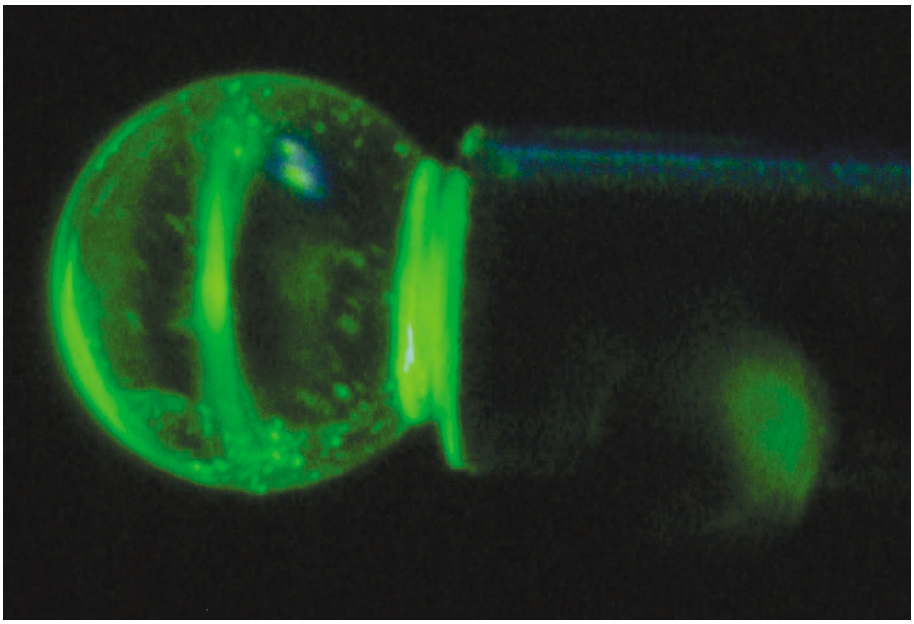

Fig. 23. – Magnified image of a microspherical resonator ($2R \cong 150\,\mu$m) in Er^{3+}-doped glass, where the up-converted light propagating in whispering gallery modes is clearly visible.

resonances as the sphere approaches the surface. We decided to further investigate this phenomenon and we analysed both the wavelength and the intensity of the emitted signal of a microspherical laser as a function of the distance from a silver or a gold mirror.

The phosphate glass used was an Er^{3+}/Yb^{3+} co-doped phosphate glass (Schott IOG-2) doped with 2% weight of Er_2O_3 and co-doped with 3% weight of Yb_2O_3. Though the use of ytterbium co-doping is traditionally associated to 980 nm pumping wavelength, we chose instead 1480 nm as the pumping wavelength, in order to obtain a good overlap between the pump and the laser mode volumes in the microsphere. Ytterbium ions were used only to reduce some of the possible drawbacks of a very high erbium concentration ($1.7 \cdot 10^{20}$ ions/cm^3), like self-pulsing or concentration quenching [197].

Spheres were produced by fusion of glass powders with a microwave plasma torch. Powders were injected axially and melt when passing through the flame, superficial tension forces giving them their spherical form. Free spheres with diameters in the range 10 to 200 μm were collected a few centimetres below. They were then glued to a stretched tip of an optical fibre ($\sim 20\,\mu$m in diameter), which in turn was mounted on a submicrometer translational stage.

To excite high-Q WGMs, light has to be launched from a phase-matched evanescent wave of an adjacent waveguide such as an angle polished or a tapered fibre or a prism under total internal reflection [198]. We used a single half-fibre-taper, which couples the pump light in the microsphere and—at the same time—allows coupling the fluorescence or laser light out of the microsphere. This half-taper was obtained by heating and stretching a standard telecommunication fibre until breaking. The drawn length was typically 850 μm, and the taper end was reduced down to 1.5 μm in diameter. The experimental set-up is sketched in fig. 24(a). The pump is a laser diode (maximum power

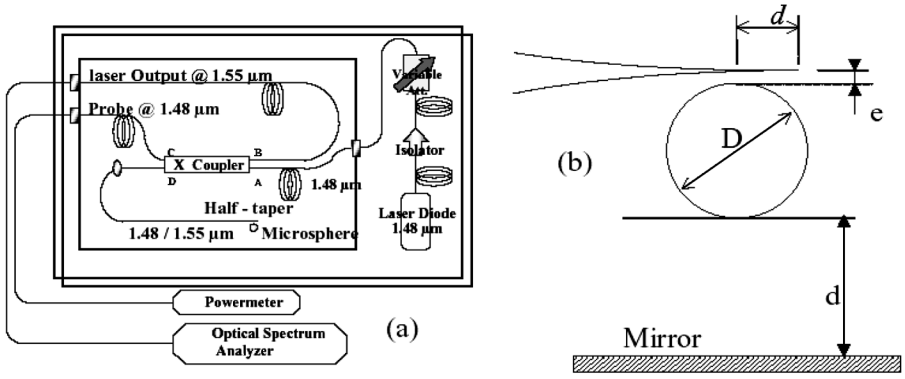

Fig. 24. – (a) Experimental set-up and (b) geometry of the coupling between the microsphere resonator and a metallic mirror.

1 W) operating around 1.48 μm. A WDM X-coupler at 1.48–1.55 μm allowed us to use the same fibre to pump and to collect the fluorescence or the laser signal. This latter was analyzed with a 70 pm resolution Optical Spectrum Analyzer (OSA). For the experiment with an external cavity, the metallic flat mirror was mounted on a microtranslational stage below the micro-sphere (fig. 24(b)).

For any sphere diameter, the optical spectrum of the laser below the threshold showed an enhancement of the fluorescence intensity and a higher peak density than those obtained coupling light with a prism, as demonstrated in a previous paper [199]. More modes can thus be excited in the sphere even above threshold. The inset of fig. 25 shows WGMs laser spectra for an isolated microsphere ($d \gg D$) with a diameter $D \sim 70\,\mu$m. Peak laser emission is obtained around 1601 nm, corresponding to a rather large gap e

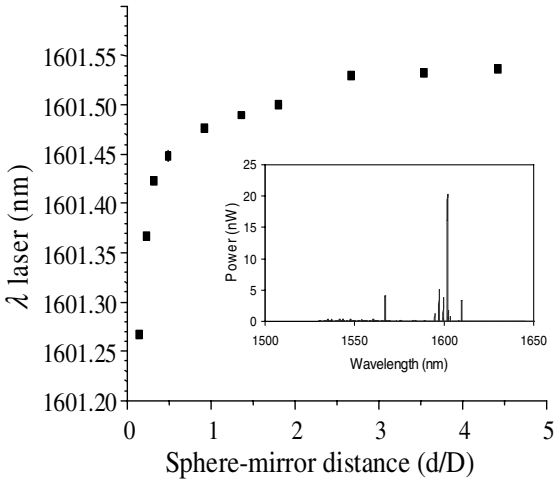

Fig. 25. – Lasing wavelength *vs.* relative sphere-to-mirror distance (d is the distance; D is the diameter of the sphere) around 1601 nm. Inset shows the multimode laser effect with the peak at 1601 nm for the isolated sphere ($D \sim 70\,\mu$m).

and a low pumping ratio. For a lower gap value, associated to a higher pumping ratio, we obtained laser effects at lower wavelengths [200].

Several papers have been written on WGMs or MDRs, but most of the research has focused on cases in which the sphere can be considered to be isolated, *i.e.* there are no strong perturbing effects from other nearby particles or surfaces. The WGMs of a sphere resting on a surface or with close neighbouring particles are also of theoretical and practical interest [199]. Johnson's theoretical treatment [196] of the MDRs of a dielectric sphere near a plane of infinite conductivity examines how the locations and widths of the resonances change as the sphere approaches the surface. If a sphere of diameter D is initially located at a distance d that is more than approximately $2D/3$ away from the point of contact with the conducting plane, the resonances will have the same locations and widths as they do in an isolated sphere. Then, as the sphere is brought closer to and eventually in contact with the surface, the locations and widths of the resonances change. Most of the change in location and width occurs when the sphere is quite close to the conducting plane. Approximately 90% of the total resonance shift occurs when the distance from the point of contact is less than 0.05 of the diameter of the sphere.

In our experiments we used a silver or gold mirror with no dielectric coating over the reflective surface. This seems to be the closest approximation to the idealized case of the perfect mirror of infinite conductivity for which the method of images is strictly valid [199]. At this point, it is important to say that with our experimental set-up, we cannot go closer to the mirror than $d = 3.5\,\mu$m. This means that, since our typical size of sphere is $D \sim 70\,\mu$m, $d_{\min}/D = 0.05$ and therefore we could not explore the zone where Johnson predicted 90% of the effect. We noticed, however, an influence of the mirror on both fluorescence and laser lines for distances up to $2.5 \times D$. Under the coupling conditions producing laser emission around 1600 nm, we moved the mirror from $d = 175\,\mu$m to $d = 7\,\mu$m. Correspondingly, we observed a line shift of almost 0.3 nm towards the lower wavelength, as shown in fig. 25, associated to an enhancement of the intensity [14]. For a lower wavelength, moving the mirror closer to the microsphere induced the same "blue shift", but also caused the laser extinction while increasing the threshold [200].

10. – Conclusions and perspectives

Photoluminescence properties of rare-earth–doped (RED) glasses are a key factor for the development of some optical components, like integrated optical amplifiers, whose characteristics are critical for achieving the flat and broad-band optical gain that seems needed in future communication systems. RED glasses are also fundamental for the development of several kinds of lasers, both in massive and integrated optics format. Erbium-doped waveguide amplifiers (EDWAs), based on Er^{3+}- or Er^{3+}/Yb^{3+}-doped glasses are already exhibiting high performances: net gains higher than 4 dB/cm and 0.15 dB/mW have been demonstrated in different oxide glasses, and commercially available devices include 1×4 and 1×8 amplified splitters/combiners, where the gain produced by the amplifier compensates the losses intrinsic to the splitting function. The search for more and more efficient compositions and guiding structures, however, is still going on. In fact, while the silica-based Er^{3+}-doped fibre amplifiers have driven the revolution in the transmission capacity of optical communication systems, further bandwidth growth will require the exploitation of new materials.

The investigation of photoluminescence properties of the RED glasses by absorption, emission, Raman and Brillouin spectroscopic techniques allowed us to increase more and

more our knowledge of their basic properties and to address the research of new materials. A few examples have been reported here, concerning glass families of great potential interest for optical communications systems. A first class is represented by SiO_2-HfO_2 binary systems: Er^{3+}-doped sol-gel planar waveguides have shown high quantum efficiency and $\approx 50\,\text{nm}$ FWHM bandwidth around $1.53\,\mu\text{m}$. A second class is constituted by soda-lime-alumino-silicate glasses, that combine the very good chemical durability of silicates and the easy waveguide fabrication process by ion exchange with the better spectroscopic properties induced by the presence of a relatively high percentage of aluminium. An increase up to 60% of the effective fluorescence bandwidth was achieved, and a high value of quantum efficiency was calculated for these glasses. Finally, Er^{3+}-doped tellurite glasses turned out to be worth of more attention, due to the broad-band emission and high emission cross-section, which can allow one to achieve higher and flatter gain than in other oxide glasses. A major problem, however, remain to be solved in tellurite glasses, namely how to efficiently manufacture channel waveguides.

We can conclude that, besides their other significant properties, rare-earth elements are of great importance in the field of optics and that there is a continuous attempt of exploiting their photoluminescence properties for the development of novel glasses, in particular aiming at the production of higher-performance broad-band integrated optical amplifiers.

* * *

We would like to thank a number of colleagues who have been collaborating with us since many years: S. Berneschi, M. Brenci, R. Calzolai, F. Cosi, G. Nunzi Conti, S. Pelli (IFAC CNR, Firenze), P. Bassi (University of Bologna), C. Armellini, A. Chiappini, A. Chiasera, Y. Jestin (IFN CNR, Trento), M. Mattarelli, M. Montagna, E. Moser, C. Tosello (University of Trento), M. Bettinelli, A. Speghini (University of Verona), P. Féron (ENSSAT - Laboratoire d'Optronique, Lannion), R. R. Gonçalves (Universidade de São Paulo, Brasil), C. Duverger (Université du Maine, Le Mans), A. Monteil (Université d'Angers), E. Duval (Université Claude Bernard, Lyon).

REFERENCES

[1] Newton Harvey N., *A History of Luminescence: From the Earliest Times Until 1900* (Dover Phoenix Editions) 2005.
[2] James F. A. J. L., *Notes and Records R. Soc. London*, **38** (1983) 79-107.
[3] `http://www.metcer.ameslab.gov/research/Complex Materials/Complex_Materials.html`.
[4] Desurvire E., *Erbium-Doped Fiber Amplifiers, Principles and Applications* (John Wiley, New York) 1994.
[5] Digonnet M. J. F., *Rare-Earth-Doped Fiber Lasers and Amplifiers* (Marcel Dekker, Inc.) 2001.
[6] Li T., *IEEE Proc.*, **81** (1993) 1568-1579.
[7] Fukuchi K., Kasamatsu T., Morie M., Ohhira R., Ito T., Sekiya K., Ogasahara D. and Ono T., *Proceedings of the Optical Fiber Communication Conference, OFC-2001*, Vol. **4** (2001) PD24-1 - PD24-3.
[8] Snitzer E., *Phys. Rev. Lett.*, **7** (1961) 444.
[9] Koester C. J. and Snitzer E., *Appl. Opt.*, **3** (1964) 1182-1186.
[10] Yajima H., Kawase S. and Sekimoto Y., *Appl. Phys. Lett.*, **21** (1972) 407-409.
[11] Saruwatari M. and Izawa T., *Appl. Phys. Lett.*, **24** (1974) 603-605.

[12] See for instance: Digonnet M. J. F. (Editor), *Selected Papers on Rare-Earth-Doped Fiber Laser Sources and Amplifiers*, Vol. MS **37** (SPIE Press, SPIE, Bellingham) 1992.
[13] Judd B. R., *Phys. Rev.*, **127** (1962) 750-761.
[14] Ofelt G. S., *J. Chem. Phys.*, **37** (1962) 511-520.
[15] Van Dijk J. M. F. and Schuurmans M. F. H., *J. Chem. Phys.*, **78** (1983) 5317-5323.
[16] Layne C. B., Lowdermilk W. H. and Weber M. J., *Phys. Rev. B*, **16** (1977) 10-21.
[17] Patek K., *Glass lasers* (Ilife Books, London) 1970.
[18] Reisfeld R. and Jorgensen C. K., *Lasers and Excited States of Rare Earths* (Springer, Berlin) 1977.
[19] Weber M., *Handbook of Laser Science and Technology* (CRC, Boca Raton) 1986-1987.
[20] Gan F., *Laser Materials* (World Scientific, Singapore) 1995.
[21] Becker P. C., Olsson, N. A. and Simpson J. R., *Erbium Doped Fibre Amplifiers: Fundamentals and Technology* (Academic Press, San Diego) 1999.
[22] Ebendorff-Heidepriem H. and Ehrt D., *Glastech. Ber. Glass. Technol.*, **71** (1998) 289-299.
[23] Yen M. W. and Selzer P. M. (Editors), *Laser Spectroscopy of Solids* (Springer, Berlin) 1981.
[24] Zschokke J. (Editor), *Optical Spectroscopy of Glasses* (Reidel, Dordrecht) 1986.
[25] Demtröder W., *Laser Spectroscopy, Basic Concepts and Instrumentation* (Springer, Berlin) 1996.
[26] Di Bartolo B., *Optical Interaction in Solids* (John Wiley & Sons Inc., New York) 1967.
[27] Menzel R., *Photonics Linear and Nonlinear Interactions of Laser Light and Matter* (Springer, Berlin) 2001.
[28] Pelli S. and Righini G. C., in *Advances in Integrated Optics*, edited by Martellucci S., Chester A. N. and Bertolotti M. (Plenum Press, New York) 1994, pp. 1-20.
[29] Tien P. K., *Rev. Mod. Phys.*, **49** (1997) 361.
[30] Ferrari M., Gonella F., Montagna M. and Tosello C., *J. Raman Spectrosc.*, **27** (1996) 793-797.
[31] Duverger C., Turrell S., Bouazaoui M., Tonelli F., Montagna M. and Ferrari M., *Philos. Mag. B*, **77** (1998) 363-372.
[32] Mendes S. B. and Saavedra S. S., *Opt. Express*, **4** (1999) 449-456.
[33] Yamamoto K. and Ishida H., *Vibrational Spectroscopy*, **8** (1994) 1-36.
[34] Grattan K. T. V. and Meggit B. T., *Optical Fiber Sensors Technology* (Chapman & Hall, London) 1995.
[35] Lavers C. R., Itoh K., Wu S. C., Murabayashi M., Mauchline I., Stewart G. and Stout T., *Sensors and Actuators B*, **69** (2000) 85-95.
[36] Lin J., *Trends Anal. Chem.*, **19** (2000) 541-552.
[37] Hocde S., Boussard-Pledel C., Fonteneau G., Lecoq D., Ma H. L. and Lucas J., *J. Non-Cryst. Solids*, **274** (2000) 17-22.
[38] Stone B. T. and Bray K. L., *J. Non-Cryst. Solids*, **197** (1996) 136-144.
[39] Duverger C., Montagna M., Rolli R., Ronchin S., Zampedri L., Fossi M., Pelli S., Righini G. C., Monteil A., Armellini C. and Ferrari M., *J. Non-Cryst. Solids*, **280** (2001) 261-268.
[40] Slooff L. H., de Dood M. J. A., van Blaaderen A. and Polman A., *J. Non-Cryst. Solids*, **296** (2001) 158-164.
[41] Marques A. C., Almeida R. M., Chiasera A. and Ferrari M., *J. Non-Cryst. Solids*, **322** (2003) 272-277.
[42] Benoit V., Bhaktha S. N., Boulard B., Chaussedent S., Chiappini A., Chiasera A., Duval E., Etienne S., Ferrari M., Gaillard-Allemand B., Jestin Y., Mattarelli M., Montagna M., Monteil A., Moser E., Nunzi Conti G., Pelli S., Portales H., Rao D. N., Righini G. C. and Vishunubhatla K. C., *Proc. SPIE*, **5723** (2005) 79-88.
[43] Houde-Walter S. N., Peters P. M., Stebbins J. F. and Zeng Q., *J. Non-Cryst. Solids*, **286** (2001) 118-131.

[44] Mandeville C. W., Webster J. D., Rutherford M. J., Taylor B. E., Timbal A. and Faure K., *Am. Mineral.*, **87** (2002) 813-821.
[45] King P. L., Vennemann T. W., Holloway J. R., Hervig R. L., Lowenstern J. B. and Forneries J. F., *Am. Mineral.*, **87** (2002) 1077-1089.
[46] Heigl J. J., Bell M. F. and White J. U., *Anal. Chem.*, **19** (1947) 293-298.
[47] Pope E. J. A. and Mackenzie J. D., *J. Non-Cryst. Solids*, **106** (1988) pp. 236-241.
[48] Davis K. M. and Tomozawa M., *J. Non-Cryst. Solids*, **201** (1996) 177-198.
[49] Innocenzi P., *J. Non-Cryst. Solids*, **316** (2003) 309-319.
[50] Bredol M., Leers D., Bosselaar L. and Hutjens M., *J. Lightwave Technol.*, **8** (1990) 1536-1540.
[51] Auzel F., *Chem. Rev.*, **104** (2004) 139-173.
[52] Potter B. G. jr. and Sinclair M. B., *J. Electroceramics*, **2-4** (1998) 295-308.
[53] Kenyon A. J., *Prog. Quantum Electron.*, **26** (2002) 225-284.
[54] Maurice E., Monnom G., Dussardier B., Saïssy A., Ostrowsky D. B. and Baxter G. W., *Appl. Opt.*, **34** (1995) 8019-8025.
[55] Dos Santos P. V., de Araujo M. T., Giuveia-Neto A. S., Medeiros Neto J. A. and Sombra A. S. B., *Appl. Phys. Lett.*, **73** (1998) 578-580.
[56] Trukhin A. N., Janson J. L. and Truhins K., *J. Non-Cryst. Solids*, **347** (2004) 80-86.
[57] Alombert-Goget G., Gaumer N., Obriot J., Rammal A., Chaussedent S., Monteil A., Portales H., Chiasera A. and Ferrari M., *J. Non-Cryst. Solids*, **351** (2005) 1754-1758.
[58] Chiasera A., Ferrari M., Mattarelli M., Montagna M., Pelli S., Portales H., Zheng J. and Righini G. C., *Opt. Mater.*, **27** (2005) 1743-1747.
[59] Campostrini R., Carturan G., Ferrari M., Montagna M. and Pilla O., *J. Mater. Res.*, **7** (1992) 745-753.
[60] Kasha M., *Discuss. Faraday Soc.*, **9** (1950) 14-19.
[61] Pucker G., Gatterer K., Frotzer H. P., Bettinelli M. and Ferrari M., *Phys. Rev. B*, **53** (1996) 6225-6234.
[62] Huber D. L., *Phys. Rev. B*, **31** (1985) 6070-6071.
[63] Huber D. L., *Mol. Cryst. Liq. Cryst.*, **291** (1996) 17-21.
[64] Kitamura T., Takahashi Y., Yamanaka T. and Uchida K., *J. Lumin.*, **48&49** (1991) 373-376.
[65] Zampedri L., Ferrari M., Armellini C., Visintainer F., Tosello C., Ronchin S., Rolli R., Montagna M., Chiasera A., Pelli S., Righini G. C., Monteil A., Duverger C. and Gonçalves R. R., *J. Sol-Gel Sci. Technol.*, **26** (2003) 1033-1036.
[66] Montagna M., in *Handbook of Sol Gel Science and Technology*, edited by Sakka S., Vol. II (Kluwer Academic Publishers, Boston) 2005, pp. 91-117.
[67] Woodward L. A., *Raman Spectroscopy* (Plenum Press, New York) 1967.
[68] Ferrari M., Montagna M., Ronchin S., Rossi F. and Righini G. C., *Appl. Phys. Lett.*, **75** (1999) 1529-1531.
[69] Barnes W. L., Laming R. I., Tarbox E. J. and Morkel P. R., *IEEE J. Quantum Electron.*, **27** (1991) 1004-1010.
[70] Duval E., Boukenter A. and Champagnon B., *Phys. Rev. Lett.*, **56** (1986) 2052-2055.
[71] Duval E., *Phys. Rev. B*, **46** (1992) 5795-5797.
[72] Montagna M. and Dusi R., *Phys. Rev. B*, **52** (1995) 10080-10089.
[73] Ceccato R., Dal Maschio R., Gialanella S., Mariotto G., Montagna M., Rossi F., Ferrari M., Lipinska-Kalita K. E. and Ohki Y., *J. Appl. Phys.*, **90** (2001) 2522-2527.
[74] Tikhomirov V. K., Furniss D., Seddon A. B., Reaney I. M., Beggiora M., Ferrari M., Montagna M. and Rolli R., *Appl. Phys. Lett.*, **8** (2002) 1937-1939.
[75] Montagna M., Moser E., Visintainer F., Ferrari M., Zampedri L., Martucci A., Guglielmi V. and Ivanda M., *J. Sol-Gel Sci. Technol.*, **26** (2003) 241-244.
[76] Ivanda M., Hohl A., Montagna M., Mariotto G., Ferrari MCrnjak Orel. Z., Turković A. and Furić K., *J. Raman Spectrosc.*, **37** (2006) 161-165.

[77] Ferrari M., in *Handbook of Sol Gel Science and Technology*, edited by Sakka S., Vol. II (Kluwer Academic Publishers, Boston) 2005, pp. 359-388.
[78] Ferrari M., Armellini C., Ronchin S., Rolli R., Duverger C., Monteil A., Balu N. and Innocenzi P., *J. Sol Gel Sci. Technol.*, **19** (2000) 569-572.
[79] Brinker C. J. and Scherer G. W., *Sol-Gel Science: The Physics and Chemistry of Sol-Gel Processing* (Academic Press) 1990.
[80] Gottardi V., Guglielmi M., Bertoluzza A., Fagnano C. and Morelli M. A., *J. Non-Cryst. Solids*, **63** (1984) 71-80.
[81] Dil J. D., *Rep. Prog. Phys.*, **45** (1982) 285-334.
[82] Shen G.-Q., Utegulov Z. N., Wicksted J. P. and Mian S. M., *Phys.-Chem. Glasses*, **43** (2002) 73-79.
[83] Montagna M., Ferrari M., Rossi F., Tonelli F. and Tosello C., *Phys. Rev. B*, **58** (1998) R547-R550.
[84] Chiasera A., Montagna M., Rossi F. and Ferrari M., *J. Appl. Phys.*, **94** (2003) 4876-4881.
[85] Chiasera A., Montagna M., Moser E., Rossi F., Tosello C., Ferrari M., Zampedri L., Caponi S., Gonçalves R. R., Chaussedent S., Monteil A., Fioretto D., Battaglin G., Gonella F., Mazzoldi P. and Righini G. C., *J. Appl. Phys.*, **94** (2003) 4882-4889.
[86] McCumber D. E., *Phys. Rev.*, **134** (1964) A229-A306.
[87] Miniscalco W. J. and Quimby R. S., *Opt. Lett.*, **16** (1991) 258-260.
[88] Payne S. A., Chase L. L., Smith L. K., Kway W. L. and Krupke W. F., *IEEE J. Quantum Electron.*, **28** (1992) 2619-2630.
[89] Quimby R. S., *J. Appl. Phys.*, **92** (2002) 180-187.
[90] Digonnet M. J. F., Murphy-Chutorian E. and Falquier D. G., *IEEE J. Quantum Electron.*, **38** (2002) 1629-1637.
[91] Rolli R., Montagna M., Chaussedent S., Monteil A., Tikhomirov V. K. and Ferrari M., *Opt. Mater.*, **21** (2003) 743-748.
[92] Desurvire E. and Simpson J. R., *Opt. Lett.*, **15** (1990) 547-549.
[93] Guy S., Bigot L., Vasilief I., Jacquier B., Boulard B. and Gao Y., *J. Non-Cryst. Solids*, **336** (2004) 165-172.
[94] Weber M. J., Myers J. D. and Blackburn D. H., *J. Appl. Phys.*, **52** (1981) 2944-2949.
[95] Feng X., Tanabe S. and Hanada T., *J. Appl. Phys.*, **89** (2001) 3560-3567.
[96] Tanabe S., *J. Non-Cryst. Solids*, **259** (1999) 1-9.
[97] Chen B. J., Righini G. C., Bettinelli M. and Speghini A., *J. Non-Cryst. Sol.*, **322** (2003) 319-323.
[98] Morrison C. A. and Leavitt R. P., *J. Chem. Phys.*, **71** (1979) 2366-2374.
[99] Leavitt R. P. and Morrison C. A., *J. Chem. Phys.*, **73** (1980) 749-757.
[100] Carnall W. T., Fields P. R. and Rajnak K., *J. Chem. Phys.*, **49** (1968) 4424-4442.
[101] Gschneidner K. A. and Eyring L., *Handbook on the Physics and Chemistry of Rare Earth*, Vol. **25** (Elsevier, Amsterdam) 1998.
[102] Weber M. J., *Phys. Rev.*, **157** (1967) 262.
[103] Condon E. U. and Shortley G. H., *The Theory of Atomic Spectra* (University Press, Cambridge) 1963.
[104] Auzel F., *J. Alloys Compounds*, **380** (2004) 9-14.
[105] Dai S. X., Yang J. H., Wen L., Hu L. and Jiang Z., *J. Lumin.*, **104** (2003) 55-63.
[106] Auzel F., Meichenin D., Mendorioz A., Balda R. and Fernandez J., *J. Lumin.*, **72-74** (1997) 152-154.
[107] Reddy K. T. R., Slifkin M. A. and Weiss A. M., *Opt. Mater.*, **16** (2001) 87-91.
[108] IUPAC Compendium of Chemical Terminology, 2nd Edition (1997) `http://www.iupac.org/publications/compendium/`
[109] Mattarelli M., Montagna M., Chiasera A., Ferrari M., Zampedri L., Righini G. C., Fortes L. M., Gonçalves M. C., Santos L. F. and Almeida R. M., *Europhys. Lett.*, **71** (2005) 394-399.
[110] Feng X., Tanabe S. and Hanada T., *J. Am. Ceram. Soc.*, **84** (2001) 165-171.

[111] Auzel F., Baldacchini G., Laversenne L. and Boulon G., *Opt. Mater.*, **24** (2003) 103-109.
[112] Noginov M. A., *Appl. Opt.*, **36** (1997) 4153-4158.
[113] Stokowski S. E., Saroyan R. A. and Weber M. J., Lawrence Livermore National Laboratory Report M-095 (1981) Rev. 2.
[114] Quimby R. S., Miniscalco W. J. and Thompson B., *J. Appl. Phys.*, **76** (1994) 4472-4478.
[115] Snoeks E., van den Hoven G. N. and Polman A., *IEEE J. Quantum Electron.*, **32** (1996) 1680-1684.
[116] Myslinski P., Nguyen D. and Chrostowski J., *J. Lightwave Technol.*, **15** (1997) 112–120.
[117] Auzel F. and Goldner P., *Opt. Mater.*, **16** (2001) 93-103.
[118] Vallés J. A., Lázaro J. A. and Rebolledo M. A., *IEEE J. Quantum Electron.*, **38** (2002) 318-323.
[119] Zhou Y., Lam Y. L., Wang S. S., Liu H. L., Kam C. H. and Chan Y. C., *Appl. Phys. Lett.*, **71** (1997) 587-589.
[120] Rocca F., Ferrari M., Kuzmin A., Dal Dosso N., Duverger C. and Monti F., *J. Non-Cryst. Solids*, **293-295** (2001) 112-117.
[121] Chiasera A., Montagna M., Rolli R., Ronchin S., Pelli S., Righini G. C., Gonçalves R. R., Messaddeq Y., Ribeiro S. J. L., Armellini C., Ferrari M. and Zampedri L., *J. Sol-Gel Sci. Technol.*, **26** (2003) 943-946.
[122] Monteil A., Chaussedent S., Alombert-Goget G., Gaumer N., Obriot J., Ribeiro S. J. L., Messaddeq Y., Chiasera A. and Ferrari M., *J. Non-Cryst. Solids*, **348** (2004) 44-50.
[123] Yablonovitch E., *Phys. Rev. Lett.*, **58** (1987) 2059-2062.
[124] Joannopoulos J. D., Meade R. D. and Winn J. N., *Photonic Crystals, Molding the Flow of Light* (Princeton University Press) 1995.
[125] Soukoulis C. M., *Photonic Crystals and Light Localization in the 21st Century* (Kluwer, Dordrecht) 2001.
[126] Purcell E. M., *Phys. Rev.*, **69** (1946) 681-681.
[127] Goy P., Raimond J. M., Gross M. and Haroche S., *Phys. Rev. Lett.*, **50** (1983) 1903-1906.
[128] Rigneault H. and Monneret S., *Phys. Rev. A*, **54** (1996) 2356-2368.
[129] Urbach H. P. and Rikken G. L. A., *Phys. Rev. A.*, **57** (1998) 3913.
[130] Vredenberg A. M., Hunt N. E. J., Schubert E. F., Jacobson D. C., Poate J. M. and Zydzik G. J., *Phys. Rev. Lett.*, **71** (1993) 517-520.
[131] Vos W. L. and Polman A., *MRS Bulletin*, **26** (2001) 642.
[132] Jacquier B., Lebrasseur E., Guy S., Belarouci A. and Menchini F., *J. Alloys Comp.*, **303-304** (2000) 207.
[133] Bellessa J., Rabaste S., Plenet J. C., Dumas J., Mugnier J. and Marty O., *Appl. Phys. Lett.*, **79** (2001) 2142-2144.
[134] Rabaste S., Bellessa J., Brioude A., Bovier C., Plenet J. C., Brenier R., Marty O., Mugnier J. and Dumas J., *Thin Solid Films*, **416** (2002) 242-247.
[135] Zampedri L., Tosello C., Portales H., Montagna M., Mattarelli M., Chiappini A., Righini G. C., Pelli S., Nunzi-Conti G., Martino M., Portal S., Marques A. C., Almeida R. M., Jestin Y., Ferrari M. and Chiasera A., *Appl. Surface Sci.*, **248** (2005) 3-7.
[136] Almeida R. M. and Portal S., *Curr. Opin. Solid State & Mater. Sci.*, **7** (2003) 151-157.
[137] Chen K. M., Sparks A. W., Luan H. C., Lim D. R., Wada K. and Kimerling L. C., *Appl. Phys. Lett.*, **75** (1999) 3805.
[138] Becker E. V., Romanova E. A., Melnikov L. A., Sinichkin Yu. P., Sorokin V. Yu., Elterman I. V., Skibina N. B., Beloglazov V. I., Sherbakov A. V., Baturin V. V., Bemson T. M. and Sewell P., *IEEE Proc. LEOS 2001*, **2** (2001) 705-706.
[139] Miller G. H., Moses E. I. and Wuest C. R., *Opt. Eng.*, **43** (2004) 2841-2853.

[140] Jeong Y., Sahu J., Payne D. and Nilsson J., *Opt. Express*, **12** (2004) 6088-6092.
[141] See, for instance, `http://www.ipgphotonics.com/html/90_1-20kw_mm_@1070nm.cfm`
[142] Hayden J. S. and Neuroth N., in Bach H. and Neuroth N. (Editors), *The Properties of Optical Glasses* (Springer Verlag, Berlin) 1998, pp. 308-324.
[143] Morito K. and Tanaka S., *Photon. Technol. Lett.*, **17** (2005) 1298–1300.
[144] Mears R. J., Reekie L., Jauncey M. and Payne D. N., *Electron. Lett.*, **23** (1987) 1026-1028.
[145] Desurvire E., Simpson J. R. and Becker P. C., *Opt. Lett.*, **12** (1987) 888-890.
[146] Yeh C.-H., Lee C.-C. and Chi S., *Photon. Technol. Lett.*, **16** (2004) 1637-1639.
[147] Vorreau P., Kilper D. C. and White C. A., *Photon. Technol. Lett.*, **17** (2005) 1405-1407.
[148] Seo H. S., Chung W. J. and Ahn J. T., *Photon. Technol. Lett.*, **17** (2005) 1181-1183.
[149] Mentzer M. A., *Principles of Optical Circuit Engineering* (Marcel Dekker, New York) 1990.
[150] Look, for instance, at these web sites: `www.teemphotonics.com, www.inplane.com`.
[151] See for instance: Silfvast W. T., *Laser Fundamentals* (Cambridge University Press, U.K.) 1998, Chapt. 3.
[152] Lumholt O., Bemas H., Chabli A., Chaumont J., Grand G. and Valette S., *Electron. Lett.*, **28** (1992) 2242-2243.
[153] Chelnokov A. V., Lourtioz J.-M., Boucaud Ph., Bernas H., Chaumont J. and Plowman T., *Electron. Lett.*, **31** (1995) 636-638.
[154] Chryssou C. E., Pitt C. W., Chandler P. J. and Hole D. E., *IEE Proc.-Optoelectron.*, **145** (1998) 325-330.
[155] Kik P. G. and Polman A., *J. Appl. Phys.*, **93** (2003) 5008-5012.
[156] Honkanen S., Najafi S. I., Poyhonen P., Orcel G., Wang W. J. and Chrostowski J., *Electron. Lett.*, **27** (1991) 2167-2168.
[157] Camy P., Roman J. E., Willems F. W., Hempstead M., van der Plaats J. C., Prel C., Beguin A., Koonen A. M. J., Wilkinson J. S. and Lerminiaux C., *Electron. Lett.*, **32** (1996) 321–323.
[158] Jiang S., Luo T., Hwang B. C., Nunzi Conti G., Myers M., Rhonehouse D., Honkanen S. and Peyghambarian N., *Opt. Eng.*, **37** (1998) 3282-3286.
[159] Kevorkian A., *Proc. SPIE*, **3289** (1998) 54-56.
[160] Righini G. C., Brenci M., Forastiere M. A., Pelli S., Ricci G., Nunzi Conti G., Peyghambarian N., Ferrari M. and Montagna M., *Philos. Mag. B*, **82** (2002) 721-734.
[161] Jose G., Sorbello G., Taccheo S., Cianci E., Foglietti V. and Laporta P., *J. Non-Cryst. Solids*, **322** (2003) 256–261.
[162] Nunzi Conti G., Tikhomirov V. K., Bettinelli M., Berneschi S., Brenci M., Chen B., Pelli S., Speghini A., Seddon A. B. and Righini G. C., *Opt. Eng.*, **42** (2003) 2805-2811.
[163] Pelli S., Bettinelli M., Brenci M., Calzolai R., Chiasera A., Ferrari M., Nunzi Conti G., Speghini A., Zampedri L., Zheng J. and Righini G. C., *J. Non-Cryst. Solids*, **345&346** (2004) 372-376.
[164] Kitagawa T., Hattori K., Shuto K., Yasu M., Kobayashi M. and Horiguchi M., *Electron. Lett.*, **28** (1992) 1818-1819.
[165] Ghosh R. N., Shmulovich J., Kane C. F., de Barros M. R. X., Nykolak G., Bruce A. J. and Becker P. C., *IEEE Photon. Technol. Lett.*, **8** (1996) 518-520.
[166] Orignac X., Barbier D., Du X. M. and Almeida R. M., *Appl. Phys. Lett.*, **69** (1996) 895-897.
[167] Martucci A., Brusatin G., Guglielmi M., Strohofer C., Fick J., Pelli S. and Righini G. C., *J. Sol-Gel Sci. Technol.*, **13** (1998) 535-539.
[168] Huang W., Syms R. R. A., Yeatman E. M., Ahmad M. M., Clapp T. V. and Ojha S. M., *IEEE Photon. Technol. Lett.*, **14** (2002) 959-961.
[169] Almeida R. M., Morais P. J. and Marques A. C., *Philos. Mag. B*, **82** (2002) 707–719.
[170] Fick J., Martucci A. and Guglielmi M., *J. Sol-Gel Sci. Technol.*, **19** (2000) 573-576.

[171] Bebbington J., Barbarossa G., Bonar J. R. and Aitchinson J. S., *Appl. Phys. Lett.*, **62** (1993) 337-339.
[172] Snoeks E., van den Hoven G. N., Polman A., Hendriksen B., Diemeer M. B. J. and Priolo F., *J. Opt. Soc. Am. B*, **12** (1995) 1468-1474.
[173] Serna R., Ballesteros J. M., Jiménez de Castro M., Solis J. and Afonso C. N., *Appl. Phys.*, **84** (1998) 2352-2354.
[174] Caricato A. P., Fernandez M., Ferrari M., Leggieri G., Martino M., Mattarelli M., Montagna M., Resta V., Zampedri L., Almeida R. M., Con M. C., Fortes L. and Santos L. F., *Mater. Sci. Eng. B*, **105** (2003) 65-69.
[175] Pérez-Casero R., Gutiérrez-Llorente A., Pons-Y-Moll O., Seiler W., Defourneau R. M., Defourneau D., Million E., Perrière E., Goldner P. and Viana B., *J. Appl. Phys.*, **97** (2005) 054905.
[176] Ozkan A. M. and Migliore L., *Proc. SPIE*, **4978** (2003) 162-168.
[177] Karnakis D. M., Knowles M. R. H., Alty K. T., Schlaf M. and Snelling H. V., *Proc. SPIE*, **5718** (2005) 216-227.
[178] Osellame R., Taccheo S., Cerullo G., Marangoni M., Polli D., Ramponi R., Laporta P. and De Silvestri S., *Electron. Lett.*, **38** (2002) 964-965.
[179] Ebendorff-Heiepriem H., *Opt. Mater.*, **25** (2004) 109-116.
[180] Sebastiani S., Nunzi Conti G., Pelli S., Righini G. C., Chiasera A., Ferrari M. and Tosello C., *Opt. Express*, **13** (2005) 1696-1701.
[181] Di Pasquale F. and Zoboli M., *J. Lightwave Technol.*, **11** (1993) 1565-1574.
[182] Chryssou, C. E., Di Pasquale, F. and Pitt, C. W., *IEEE J. Select. Topics Quantum Electron.*, **6** (2000) 114-121.
[183] D'Orazio A., De Sario M., Mescia L., Petruzzelli V., Prudenzano F., Chiasera A., Montagna M., Tosello C. and Ferrari M., *J. Non-Cryst. Solids*, **322** (2003) 278–283.
[184] Zampedri L., Righini G. C., Portales H., Pelli S., Nunzi Conti G., Montagna M., Mattarelli M., Goncalves R. R., Ferrari M., Chiasera A., Bouazaoui M. and Armellini C., *J. Non-Cryst. Solids*, **345&346** (2004) 580-584.
[185] Goncalves R. R., Carturan G., Ferrari M., Zampedri L., Montagna M., Pelli S., Righini G. C., Ribeiro S. J. L. and Messaddeq Y., *Opt. Mater.*, **25** (2004) 131-140.
[186] Wong S. F., Pun E. Y. B. and Chung P. S., *IEEE Photon. Technol. Lett.*, **14** (2002) 80-82.
[187] Hehlen M. P., Cockroft N. J., Gosnell T. R. and Bruce A. J., *Phys. Rev. B*, **56** (1997) 9302-9318.
[188] Berneschi S., Bettinelli M., Brenci M., Nunzi Conti G., Pelli S., Sebastiani S., Siligardi C., Speghini A. and Righini G. C., *J. Non-Cryst. Solids*, **351** (2005) 1747-1753.
[189] Nunzi Conti G., Tikhomirov V. K., Bettinelli M., Berneschi S., Brenci M., Chen B., Pelli S., Speghini A., Seddon A. B. and Righini G. C., *Opt. Eng.*, **42** (2003) 2805-2811.
[190] Vahala K. J., *Nature*, **424** (2003) 839-846.
[191] Garret C. G. B., Kaiser W. and Long W. L., *Phys. Rev.*, **124** (1961) 1807.
[192] Barber P. W. and Chang R. K., *Optical Effects Associated with Small Particles* (World Scientific, Singapore) 1988.
[193] Sandoghdar V. S., Treussart F., Hare J., Lefèvre-Seguin V., Raimond J. M. and Haroche S., *Phys. Rev. A*, **54** (1996) 1777.
[194] Lissillour F., Feron P., Dubreuil N., Dupriez P., Poulain M. and Stephan G., *Electron. Lett.*, **36** (2000) 1382.
[195] Righini G. C., Arnaud C., Berneschi S., Bettinelli M., Brenci M., Chiasera A., Feron P., Ferrari M., Montagna M., Nunzi Conti G., Pelli S., Portales H., Siligardi C., Speghini A. and Zampedri L., *Opt. Mater.*, **27** (2005) 1711-1717.
[196] Johnson B. R., *J. Opt. Soc. Am. A*, **11** (1994) 2055.
[197] Ohtsuki T., Honkanen S., Najafi S. I. and Peyghambarian N., *J. Opt. Soc. Am. B*, **14** (1997) 1838.

[198] Ilchenko V. S., Yao X. S. and Maleki L., *Opt. Lett.*, **24** (1999) 723.
[199] Lissillour F., Messager D., Stéphan G. M. and Féron P., *Opt. Lett.*, **26** (2001) 1051.
[200] Arnoud C., Boustimi M., Féron P., Nunzi Conti G. and Righini G., *SPIE Proc.*, **5333** (2004) 140.